

“Babeş-Bolyai” University Cluj-Napoca
Faculty of Physics

PhD. Thesis Summary

**Magnetic Properties of $3d$ Transition
Metals in Intermetallic Compounds
and Oxides**

Scientific Supervisor:
Prof. Dr. Romulus V. Tetean

PhD. Student:
Sever Mican

Cluj-Napoca, 2012

Contents

Introduction	iii
1 Rare Earth - 3d Transition Metal Intermetallic Compounds	1
1.1 Definition	1
1.2 Crystal Structure	1
1.3 Magnetic Properties	3
2 Rare Earth - 3d Transition Metal Oxides	4
2.1 Crystal Structure	4
2.2 Magnetic Properties	5
3 Experimental and Computational Methods	6
3.1 Preparation Aspects	6
3.2 X-Ray Photoelectron Spectroscopy	7
3.3 Structural and Morphological Techniques	8
3.4 Magnetic Measurements	8
3.5 Computational Methods	9
4 Magnetic Properties of Rare Earth - 3d Transition Metal Intermetallic Compounds	9
4.1 Magnetic Properties and MCE in $\text{La}_{0.7}\text{Nd}_{0.3}\text{Fe}_{13-x}\text{Si}_x$ Compounds	9
4.2 Magnetism and Large MCE in $\text{HoFe}_{2-x}\text{Al}_x$ Compounds	13
4.3 Magnetic Behaviour of Fe in $\text{Er}_{1-x}\text{Zr}_x\text{Fe}_2$ Compounds	18
5 Magnetic Properties of Rare Earth - 3d Transition Metal Oxides	22
5.1 Magnetic Properties and MCE in $\text{La}_{1.4-x}\text{Ce}_x\text{Ca}_{1.6}\text{Mn}_2\text{O}_7$ Perovskites Synthesized Through the Sol-Gel Method	22
5.2 Effects of the Pr, Nd, Sm and Gd Substitution for La on the Magnetic Properties of $\text{La}_{1.4}\text{Ca}_{1.6}\text{Mn}_2\text{O}_7$	27
Selected Conclusions	32
Selected References	34
List of Publications	38
List of Conference Contributions	39
Acknowledgements	41

Keywords: intermetallic compounds, double layered manganites, magnetic entropy change, magnetic measurements

Introduction

The magnetocaloric effect (MCE), displaying itself as the generation or absorption of heat by a magnetic material under the action of a magnetic field, has attracted a lot of attention in recent years due to the fact that a series of acting magnetic refrigerator prototypes have been developed, with a certain number of them working at room temperature, therefore having a significant potential to be incorporated into the marketplace [1]. Magnetic refrigerators are characterized by compactness, high effectiveness, low energy consumption and environmental safety. One of the most important parts of the magnetic refrigerator is its magnetic working body, which should have high magnetocaloric properties, in particular, a high MCE value [2].

Among materials with high magnetocaloric properties, rare earth-3*d* transition metal (*R-M*) intermetallic compounds and oxides were suggested as being promising candidates for magnetic refrigeration applications. *R-M* intermetallic compounds are of particular interest due to the fact that one can benefit from the high magnetic moment per atom and the strong single-ion magnetocrystalline anisotropy of the rare earths and the high magnetic coupling strength of the moments of the 3*d* transition metals [3]. The $R_{2-2x}A_{1+2x}Mn_2O_7$ double-layered manganites (where $R = \text{La, Pr, Nd etc.}$ and $A = \text{Sr, Ca or Ba}$), have attracted much interest due to the intriguing properties displayed by these materials and the fact that their physical properties are sensitive to small changes in composition and structure.

This work is divided into five chapters. The first three chapters cover the fundamentals of intermetallic compounds (chapter 1) and oxides (chapter 2), along with a short description of the experimental and computational techniques used in the investigations (chapter 3). In Chapter 4, the magnetic properties of rare earth-3*d* transition metal intermetallic compounds are investigated. Some physical properties of $\text{La}_{0.7}\text{Nd}_{0.3}\text{Fe}_{13-x}\text{Si}_x$, $\text{HoFe}_{2-x}\text{Al}_x$ and $\text{Er}_{1-x}\text{Zr}_x\text{Fe}_2$ intermetallic compounds were studied in a wide composition range. This chapter focuses on the effects of various substitutions on the structural, magnetic and magnetocaloric properties of these materials, along with a detailed discussion on the possibilities of using these materials in magnetic refrigeration applications. Chapter 5 treats the effects of substituting La with Ce, Pr, Sm, Nd and Gd on the magnetic properties and magnetocaloric effect of $\text{La}_{1.4}\text{Ca}_{1.6}\text{Mn}_2\text{O}_7$ double-layered manganites prepared through a direct sol-gel method. Along with discussions on the magnetic and magnetocaloric properties these materials, we also raise the question of using these materials in magnetic refrigeration devices.

Chapter 1

Rare Earth - 3d Transition Metal Intermetallic Compounds

1.1 Definition

If two metals, A and B , are alloyed, three possibilities exist. The first possibility is one where the two metals may not mix in the solid state, A and B being present as separate phases. The second possibility is one where the two metals form a solid solution over a certain range of compositions. The physical properties of the mixture generally agree with those expected on the basis of a linear interpolation between the properties of the parent materials [3]. The third possibility is that where the alloying of the two metals leads to the formation of intermetallic compounds. These compounds are characterized by well-defined stoichiometric compositions (AB_2 , AB_5 , AB_{13} etc.). The physical properties of these compounds need not have anything in common with the physical properties of the composing elements [3].

1.2 Crystal Structure

The intermetallic compounds in the RM_2 class can crystallize either in the $MgCu_2$ or the $MgZn_2$ structure types which originate from the hexagonal $CaCu_5$ structure [4]. The $MgCu_2$ (C15) structure is cubic, while the $MgZn_2$ (C14) structure is hexagonal [4, 5]. The ideal C15 (figure 1.1) and C14 (figure 1.2) structures are very similar, the only difference being a slightly different stacking arrangement of the $CaCu_5$ blocks [4]. The R atoms in both cases are stacked as tetrahedra, joined alternatively point-to-point and base-to-base in the cubic structure and point-to-point in the hexagonal structure [4]. The $MgCu_2$ structure is cubic (space group $Fd\bar{3}m$), having eight formula units per cell. The R atoms are placed in position $8a$, while the M atoms are situated in position $16d$ [5]. The $MgZn_2$ structure type is hexagonal (space group $P6_3/mmc$) and contains four formula units per cell. The R atoms are placed in position $4f$, while two of the M atoms are placed in position $2a$ and the remaining six M atoms are placed in position $6h$ [5]. The RM_{13} compounds have the $NaZn_{13}$ -type structure, which is face-centered cubic with 112 atoms per unit cell (figure 1.3) [7]. The space group is $Fm\bar{3}c$. The compounds which crystallize in this structure have the R atoms in positions $8a$ surrounded by a nearly regular snub cube of 24 M_I atoms occupying positions $96i$ [7]. The M_{II} atoms are in position $8b$,

¹The crystal structures were drawn using the VESTA software – see [6]

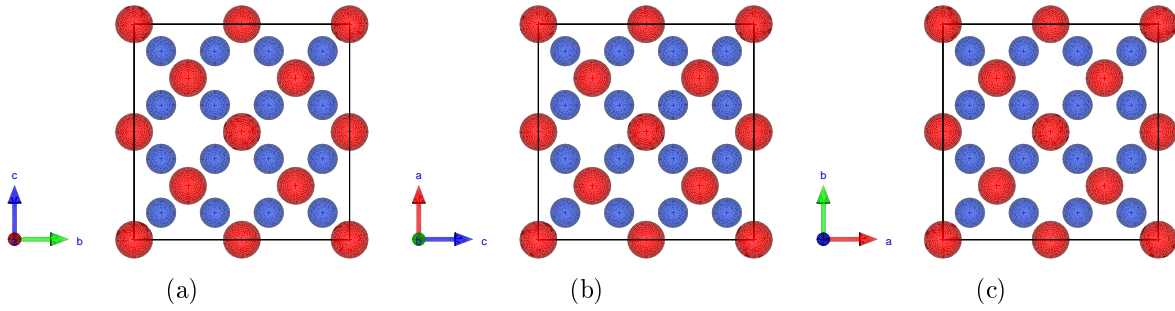


Figure 1.1: Unit cell for the cubic MgCu_2 (C15) structure: viewed along the a -axis (a), the b -axis (b) and c -axis (c). R and M atoms are represented by red and blue spheres respectively.¹

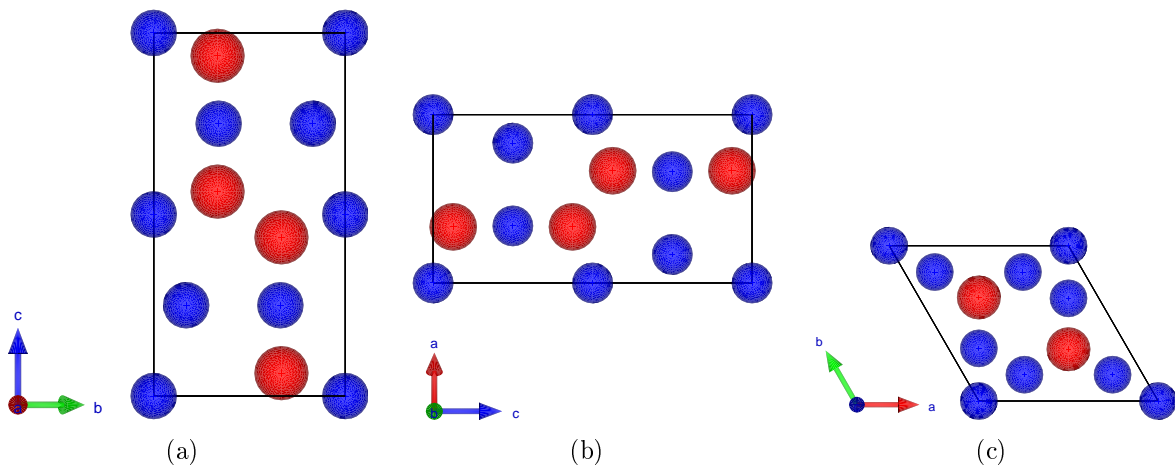


Figure 1.2: Unit cell for the hexagonal MgZn_2 (C14) structure viewed along the a -axis (a), the b -axis (b) and c -axis (c). R and M atoms are represented by red and blue spheres respectively.¹

surrounded by a nearly regular icosahedron of M_I atoms [7].

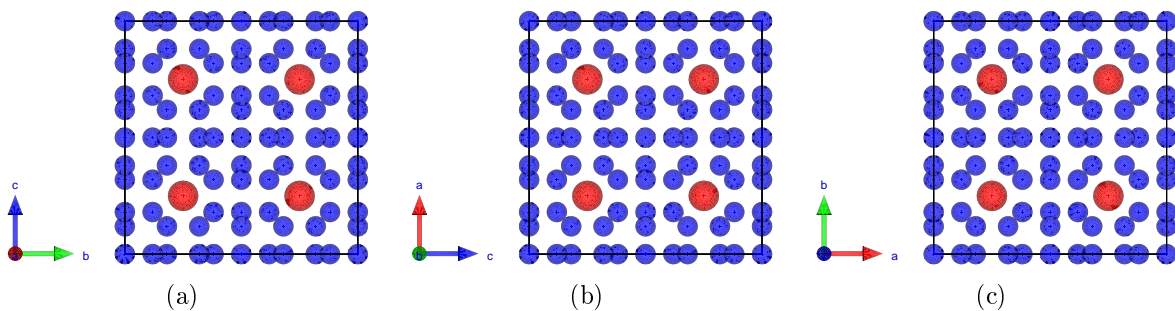


Figure 1.3: Unit cell for the cubic NaZn_{13} structure viewed along the a -axis (a), the b -axis (b) and c -axis (c). R and M atoms are represented by red and blue spheres respectively.¹

¹The crystal structures were drawn using the VESTA software – see [6]

1.3 Magnetic Properties

In R - M compounds, the following magnetic interactions occur: the R - R interaction, the M - M interaction and the R - M interaction [3]. The interaction between the R atoms is by far the weakest one [3]. Due to the small spatial extent of the $4f$ wavefunction, the interaction is realized through the spin polarization of the s -conduction electrons [3]. This type of interaction is generally referred to as Ruderman-Kittel-Kasuya-Yosida (RKKY) interaction. It has an oscillatory character and its absolute value decreases with increasing distance [3].

The M - M interaction is much stronger [3]. This is a direct consequence of the larger spatial extent of the $3d$ wavefunctions compared to the $4f$ ones. The large spatial extent of the $3d$ wavefunctions implies that wavefunctions of neighboring atoms show a strong overlap. This leads to $3d$ -electron energy bands rather than to $3d$ levels. It is also possible for the $3d$ electrons to move through the whole lattice like conduction electrons [3]. The itinerant electron model, in its simplest form, predicts an exchange splitting between the two $3d$ sub-bands, and hence a magnetic moment, if the Stoner criterion is satisfied [8]:

$$IN(E_F) - 1 \equiv \tilde{I} - 1 > 0 \quad (1.1)$$

where I is the effective Coulomb repulsion between the $3d$ electrons and $N(E_F)$ is the $3d$ -electron density of states at the Fermi level.

The magnetic interaction between the R and M moments has a strength intermediate between the two types of interactions discussed above [3]. The saturation moments of the R - M compounds in which R as well as M carry a magnetic moment can be interpreted as being the results of antiparallel coupling between the R and M sublattices if R is a heavy rare earth element and parallel coupling if R is a light rare earth element [3]. Furthermore, if the saturation magnetization of the R sublattice exceeds that of the M sublattice, the compounds with heavy rare-earth elements exhibit a compensation point in the temperature dependence of the magnetization [3]. The observed differences between compounds in which R is a light or heavy rare earth element follows from the fact that in the former the total rare earth angular momentum is given by $J = L - S$ while in the latter it is given by $J = L + S$ [3].

Chapter 2

Rare Earth - 3d Transition Metal Oxides

2.1 Crystal Structure

The crystal structures of the oxides studied in this work are based on the perovskitic structure. The perovskitic structure is characteristic for materials which have the chemical formula ABO_3 . The ideal perovskite structure is cubic (space group $Pm\bar{3}m$) [9] and can be viewed as being made up of large A cations in the corners, the B cation in the center and the oxygen ions in the centers of the the cube faces [10] – figure 2.1.

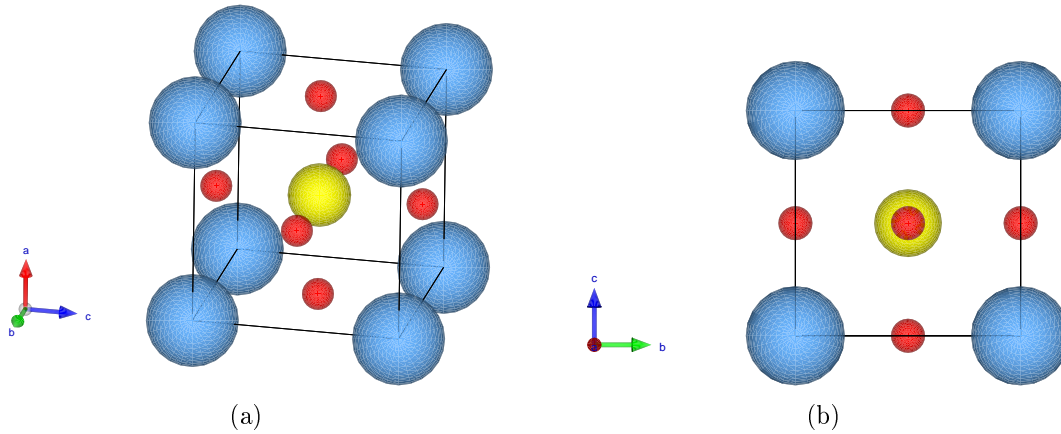


Figure 2.1: (a) the ideal cubic perovskite structure; (b) the ideal cubic perovskite structure viewed along the a -axis. The blue spheres represent the A atoms, the yellow spheres represent the B atoms, and the red spheres represent the O atoms. ¹

Even though the ideal perovskite structure is cubic, recent studies suggest that many perovskites crystallize in the orthorhombic $Pnma$ (such as $CaTiO_3$) [11, 12] or $Pbnm$ [13, 14] distorted structures at room temperature. Other further distortions are possible resulting in a rhombohedral structure (space group $R\bar{3}c$) [9, 15, 16] or a hexagonal one (space group $P6_3cm$) [10, 12].

It was reported previously that not only three-dimensional, but also layered structures of perovskites can occur [17]. The oxidic compounds studied in this work are double-layered perovskites which are part of the Ruddlesden-Popper $A_{n+1}B_nO_{3n+1}$ homologous series [18]. The structure of the Ruddlesden-Popper phases consists of blocks built up from perovskite-like sheets of vertex-sharing MnO_6 octahedra, each block being infinite in two dimensions (xy) and n layers thick in the third (z) – figure 2.2. Several members

¹The crystal structures were drawn using the VESTA software – see [6]

of the layered perovskite family, including the compounds studied in this work, crystallize in a tetragonal structure (space group $I4/mmm$) [19, 20], like the one of $\text{Sr}_3\text{Mn}_2\text{O}_7$ [21].

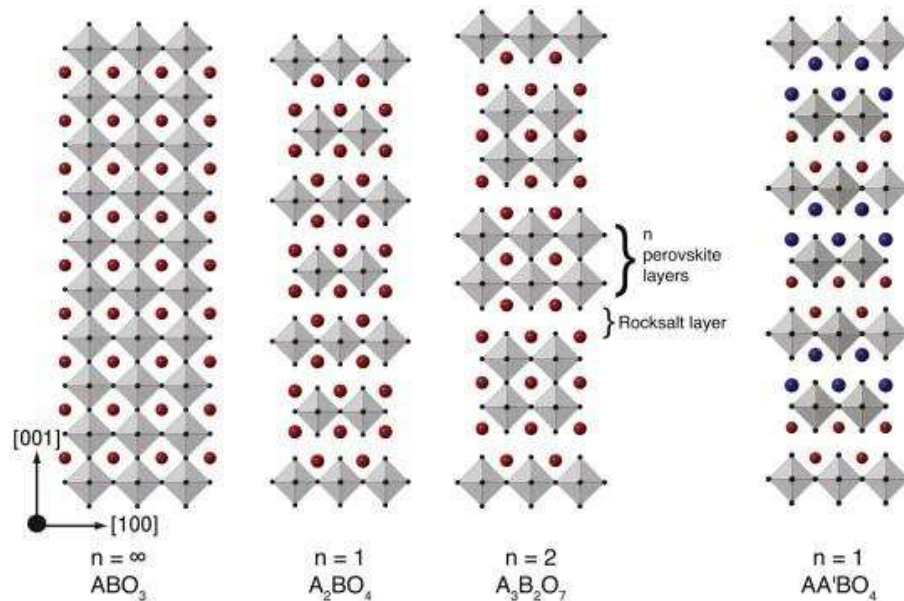


Figure 2.2: The Ruddlesden-Popper $A_{n+1}B_nO_{3n+1}$ homologous series and an A -site ordered $n = 1$ Ruddlesden-Popper phase ($AA'BO_4$) built from two different A -site cations [22].

2.2 Magnetic Properties

The mixed-valence manganites can exhibit magnetic order, charge order and orbital order [23]. The two types of exchange interactions which are relevant in these materials are double exchange and superexchange. Whenever different ions of the same $3d$ element with different numbers of electrons occupy the B sites, there is a partly-filled d band with a tendency towards metallic conduction [23]. Zener [24] explained this behaviour in terms of his theory of indirect magnetic exchange, called double exchange, between $3d$ atoms. Double exchange associates the appearance of ferromagnetic coupling of the localized magnetic moments (in the t_{2g} energy level) to the delocalization of an e_g electron [25]. In other words, the double exchange interaction is the simultaneous transfer of an electron from the Mn^{3+} ion to the oxygen ion and from the oxygen ion to the neighbouring Mn^{4+} ion [23]. Zener [24] considered that the intra-atomic Hund rule exchange was strong and that the electrons do not change their spin orientation when hopping from one ion to the next, therefore they can only hop if the spins of the two ions are parallel [23].

Magnetic coupling in many magnetic oxides cannot be described by the direct exchange mechanism due to the fact that the ions are too far apart [25]. Furthermore, the magnetic ions are often separated by nonmagnetic ones, like oxygen [25]. Kramers [26] and later

Anderson [27, 28] proposed a mechanism through which the magnetic moments of the magnetic cations are coupled indirectly through intermediate anions [25]. This exchange mechanism is called superexchange. Superexchange is based on the energy minimization for the transfer of a virtual electron from the full oxygen p shell to the excited states of neighbouring magnetic ions. [25]. This process can be treated as a perturbation of the Heisenberg Hamiltonian [25]:

$$H = \sum_{i,j} J_{ij} \vec{S}_i \vec{S}_j \quad (2.1)$$

where S_i and S_j are the localized moments on the magnetic ions and J_{ij} is the exchange interaction. The exchange interaction term, J_{ij} , is difficult to calculate and its sign depends on the geometry of the involved orbitals [25]. The exchange interaction term can be approximated by t^2/U [25], where t is the hopping integral for the transfer of an electron from oxygen to a neighbouring magnetic ion and U is the Coulomb energy which must be paid in order to add an electron to a singly occupied magnetic orbital. Hopping of the $3d$ electrons occurs via the $2p$ oxygen orbitals. The $3d$ orbitals can be coupled via the oxygen $2p$ orbital in three different ways (when the angle of the M-O-M bond is 180°), which are described by the Goodenough-Kanamori rules [29, 30]:

1. Coupling between cations with half-filled e_g orbitals is antiferromagnetic (AFM)
2. Coupling between cations with half-filled t_{2g} orbitals is weakly antiferromagnetic (AFM)
3. Coupling between a cation with a half-filled t_{2g} orbital with one with half-filled e_g orbital is ferromagnetic (FM)

Chapter 3

Experimental and Computational Methods

3.1 Preparation Aspects

3.1.1 The Arc-Melting Method

Rare earth - transition metal intermetallic compounds are usually prepared through arc melting or induction melting of the stoichiometric proportions of the starting materials. Arc melting is conducted in a cold-wall system using an inert atmosphere, usually argon, at reduced pressure. The cathode may either be inert (made up of tungsten) or

consumable, in which case it is made up of either the product compound or a composite of the component materials [31]. The arc is produced by a stream of electrons emitted from the cathode and drawn through a plasma of ionized gas to a water-cooled copper anode in the form of a crucible or hearth. Temperatures of up to 3000°C can be easily attained through this technique; therefore all intermetallics can be melted using this method [31].

3.1.2 The Sol-Gel Method

The sol-gel process is a wet chemical technique, known also as chemical solution deposition. This technique allows us to change the composition and structure of materials on the nanometer scale [32]. In the sol-gel method, stoichiometric amounts of the starting materials (oxides and nitrates) are dissolved in distilled water or concentrated nitric acid. The individual solutions are mixed together and an aqueous solution of citric acid and ethylene glycol are added. It is very important that the pH value remains lower than 7, since at higher pH values, hydroxides and base salts will appear. The resulting clear solution is heated until a gel-type solution is obtained. The gel is then decomposed in air at temperatures below 300° C until a fine homogeneous powder is obtained. The decomposed powders are heated in air at high temperatures (usually between 700°C and 1100°C) for several hours. The citrate-gel has potential advantages over other methods not only for achieving homogeneous mixing of components on the atomic scale, but also for the possibility of forming films which are of technological importance.

3.2 X-Ray Photoelectron Spectroscopy

The XPS spectra were recorded using a PHI 5600ci ESCA spectrometer with monochromatized Al K_{α} radiation at room temperature. The pressure in the ultra-high vacuum chamber was in the 10^{-10} mbar range during the measurements. XPS spectra can provide important information on the electronic structure of manganese double-layered perovskites. Core level photoelectron spectroscopy is sensitive to the chemical environment and can give information about the oxidation state of the probed ion. In manganites, the valence state of the Mn ions can be investigated by means of Mn 3s core level XPS due to the spectral splitting of the 3s core level mediated by the exchange coupling between the 3s hole and the 3d electrons [33]. The magnitude of the splitting is proportional to $(2S + 1)$, where S is the local spin of the 3d electrons in the ground state. The Mn valence in bulk mixed-valent manganites can be estimated based on the measured Mn 3s core level splitting, ΔE_{ex} , according to the linear equation obtained by [34]:

$$\nu_{\text{Mn}} = 9.67 - 1.27\Delta E_{\text{ex}}/eV \quad (3.1)$$

3.3 Structural and Morphological Techniques

The crystal structure of the samples was investigated using powder X-Ray diffraction. The powder diffraction data was recorded as intensity versus Bragg angle. The samples were ground to a fine powder which was analyzed at room temperature on a Brüker D8 Advance diffractometer using Cu K_α and Cr K_α radiation in the Bragg-Brentano focusing geometry. The lattice parameters and phase percentages were determined using the FullProf software.

The morphological and compositional characterization was performed using Transmission Electron Microscopy and Scanning Electron Microscopy coupled with Energy Dispersive X-Ray Spectroscopy. The SEM-EDS studies were performed on the pressed pellets with a Jeol-JSM 5800LV microscope equipped with an EDX spectrometer. For transmission electron microscopy, the samples were obtained by suspending the powder in ethanol and depositing it onto a gold grid with a holey carbon layer and investigated using a 200kV-High Resolution Transmission Electron Microscope (HRTEM) Philips CM 20 FEG with an Imaging Energy Filter from Gatan (GIF). The crystallinity of the samples was investigated using Selected Area Electron Diffraction (SAED).

3.4 Magnetic Measurements

3.4.1 The Magnetocaloric Effect

The magnetocaloric effect (MCE) displays itself as the production or absorption of heat by a magnetic material under the action of a magnetic field [2]. In order to characterize the MCE in a given material, the physical quantities of interest are the magnetic entropy change, ΔS_M , the relative cooling power, RCP .

The magnetic entropy change can be determined from experimental data on magnetization isotherms, $M(H)$, by using the following equation [2]:

$$|\Delta S_M| = \sum_i \frac{M_i - M_{i+1}}{T_{i+1} - T_i} \Delta H_i \quad (3.2)$$

The relative cooling power, RCP , takes into account not only the magnitude of the magnetocaloric effect (ΔT_{ad} and ΔS_M), but also the width of the $\Delta S_M(T)$ curves [2]. The relative cooling power based on the magnetic entropy change has the following form [2]:

$$RCP(S) = -\Delta S_M(\max) \cdot \delta T_{FWHM} \quad (3.3)$$

3.4.2 Instrumentation Used for Magnetic Measurements

The magnetic investigations were performed using a vibrating sample magnetometer (VSM) and a horizontal Weiss Balance. The VSM measurements were performed using a VSM made by Cryogenic Limited in the 4.2-700 K temperature range in applied magnetic fields up to 12 T. With the Weiss balance we performed measurements at temperatures above room temperature (300-1300 K) in external applied fields up to 1 T. For the magnetic investigations, DC magnetization and susceptibility measurements were performed.

3.5 Computational Methods

The electronic structure of the investigated compounds was calculated self-consistently by means of the spin polarized relativistic Korringa-Kohn-Rostoker (SPR-KKR) and LMTO (LSDA+U) methods in the atomic sphere approximation (ASA) mode using the experimentally determined lattice parameters. In the KKR method, exchange and correlation effects were treated within the framework of the local density approximation, using the parametrization of Vosko et al. [35]. For integration over the Brillouin zone, the special points method was used [36]. The substitutional disorder in the system has been accounted for by means of the Coherent Potential Approximation (CPA) [37, 38].

The electronic structure computed using the LMTO method were performed using a supercell eight times greater than the conventional unit cell. A *d-f*-type model was used in the mean field approximation, in which the Fe 3*d* and Er 4*f* states were described by LSDA+U method, where the 3*d*-4*f* interaction was treated as perturbation.

Chapter 4

Magnetic Properties of Rare Earth - 3*d* Transition Metal Intermetallic Compounds

4.1 Magnetic Properties and MCE in $\text{La}_{0.7}\text{Nd}_{0.3}\text{Fe}_{13-x}\text{Si}_x$ Compounds

Among magnetic materials with high magnetocaloric properties, the NaZn_{13} -type $\text{LaFe}_{13-x}\text{Si}_x$ system was suggested to be a good candidate for near-room-temperature magnetic refrigeration due to the high MCE values reported for these materials [1, 2, 39–50] and due to the fact that their transition temperature can be easily modified by adjusting the dopant concentration [39, 42–44, 48, 49]. These compounds display large entropy

change values due to the first-order character of the transition at T_C [45]. A changing of the transition character with increasing Si content was reported, along with the presence of an IEM transition for the compounds with low Si content in the paramagnetic region [39, 39, 46, 50, 51] which causes a hysteresis loop above a critical field, H_C [46]. Considering the promising results obtained for $\text{La}_{0.7}\text{Nd}_{0.3}\text{Fe}_{11.5}\text{Si}_{1.5}$ [52], we investigated the structural, magnetic and magnetocaloric properties of $\text{La}_{0.7}\text{Nd}_{0.3}\text{Fe}_{13-x}\text{Si}_x$ in a wide composition range ($1.2 \leq x \leq 1.8$) using X-Ray diffraction and magnetic measurements.

All of the prepared $\text{La}_{0.7}\text{Nd}_{0.3}\text{Fe}_{13-x}\text{Si}_x$ compounds crystallized in a cubic NaZn_{13} -type structure. The lattice parameters obtained from XRD patterns are weakly dependent on silicon content – table 4.1. The presence of a small α -Fe phase was detected which decreases in amount with Si content. In the hypothetical LaFe_{13} structure, the La atoms occupy the $8a$ site, while the Fe atoms are located on the $8b$ and $96i$ sites. From the analysis of ^{57}Fe Mössbauer spectra, Hamdeh et al. [53] have concluded that Si atoms occupy the $96i$ sites only.

Table 4.1: Lattice parameters and phase concentrations for the investigated $\text{La}_{0.7}\text{Nd}_{0.3}\text{Fe}_{13-x}\text{Si}_x$ compounds.

x	a (Å)	NaZn_{13} phase (%)	α -Fe phase (%)
1.2	11.45(9)	94	6
1.4	11.46(1)	95.9	4.1
1.6	11.45(7)	97.9	2.1
1.8	11.45(8)	98.8	1.2

Evidence of thermal hysteresis was found in all the samples, indicating the presence of a thermally-induced first-order magnetic transition at the Curie temperature (T_C). The thermal hysteresis decreases with Si content from 9 K for $x = 1.2$ to 5 K for $x = 1.8$, implying that the increase of silicon content weakens the thermally-induced first-order magnetic transition at T_C as was previously reported for Pr-doped compounds [54]. The T_C values increase linearly with Si concentration from 181 K ($x = 1.2$) to 213 K ($x = 1.8$) – table 4.2. In these compounds, the Curie temperature is mainly determined by the Fe-Fe and R -Fe interactions, but generally, the Fe-Fe interactions are dominant. In our compounds, the increase of T_C with Si concentration is due to a decrease of the total DOS at the Fermi level caused by the substitution of Si for Fe as was reported in [55] and [56].

These compounds were found to be ferromagnetically ordered, with a parallel orientation of the the Nd and Fe moments. All the samples reach saturation in external applied fields of 2 T. The saturation moments at 5 K decrease with Si content from $26.7 \mu_B/\text{f.u.}$ for $x = 1.2$ to $23.7 \mu_B/\text{f.u.}$ for $x = 1.8$, a behaviour consistent with ferromagnetic order. Considering that the Nd moment equal to that of the Nd^{3+} ion the iron magnetic

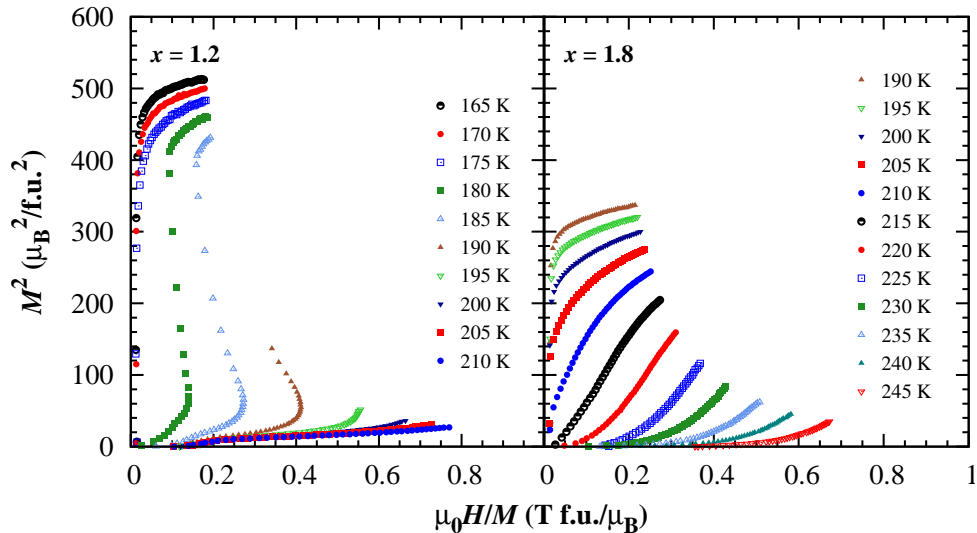


Figure 4.1: Arrot plots for the investigated $\text{La}_{0.7}\text{Nd}_{0.3}\text{Fe}_{13-x}\text{Si}_x$ compounds.

moment was determined and it was found to be quite independent of composition, being $2.05 \pm 0.09 \mu_{\text{B}}/\text{atom}$, suggesting a high degree of localization. It is possible that in our compounds La has a magnetic moment value in the range $0.38\text{-}0.45 \mu_{\text{B}}/\text{atom}$ [57], therefore a variation of the Fe moment of $0.02 \mu_{\text{B}}/\text{atom}$ can be expected.

The presence of negative slope values in the Arrot plots for the compounds with lower Si content shows that these samples undergo a first-order magnetic phase transition from a ferromagnetic to a paramagnetic state at T_{C} – figure 4.1. The presence of an inflexion point in the Arrot plots shows that these samples also undergo an IEM transition above T_{C} . The increase in Si content weakens the IEM transition, and in the case of the sample with $x = 1.8$ the IEM transition is not present. However, the presence of thermal hysteresis

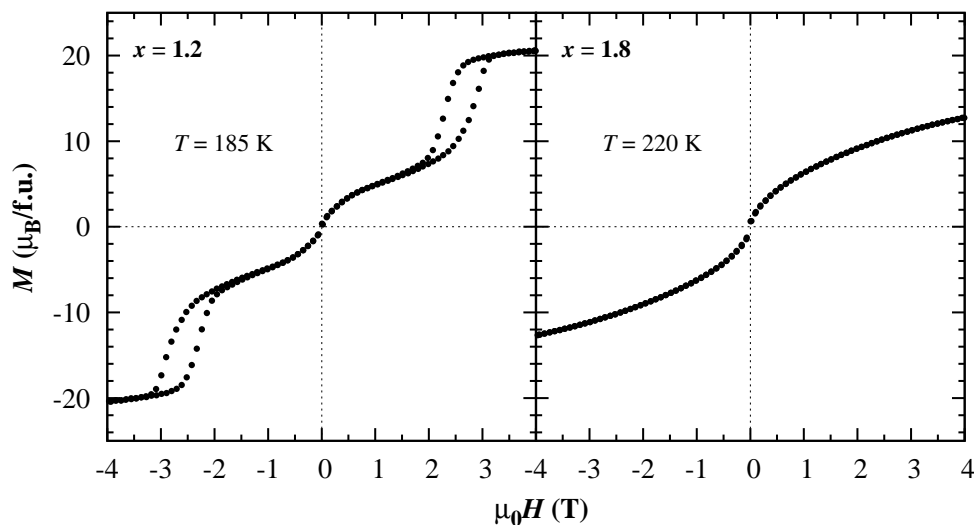


Figure 4.2: Magnetic hysteresis loops for $\text{La}_{0.7}\text{Nd}_{0.3}\text{Fe}_{13-x}\text{Si}_x$.

at the transition leads us to believe that the compound with $x = 1.8$ undergoes a weak first-order transition at T_C .

No magnetic hysteresis above the transition temperature was found for external magnetic fields lower than 2 T in all cases, as it is expected for the paramagnetic region – figure 4.2. This is important for magnetic refrigeration, considering that in commercial applications, applied fields produced by permanent magnets do not exceed 2 T. In the case of the samples which present an IEM transition, the magnetic hysteresis can be seen in higher applied fields.

The maximum obtained entropy change values were found to decrease from 28.7 J/kgK for $x = 1.2$ to 12.6 J/kgK for $x = 1.8$ for a magnetic field change from 0 to 4 T. The large ΔS_M values obtained for the samples with low Si content are mainly due to the first-order character of the transition at T_C . Also, the field-induced transition above T_C causes an asymmetric broadening of the $\Delta S_M(T)$ peak towards higher temperatures for higher applied fields – figure 4.3. With increasing Si content, the first-order character of the transition at T_C is diminished, leading to lower ΔS_M values. It is worthwhile to note that the maximum entropy change decreases only to 27 J/kgK for $x = 1.2$ and to 7.9 J/kgK for $x = 1.8$ respectively, in external magnetic field changes of 0-2 T, which is very important for magnetic refrigeration.

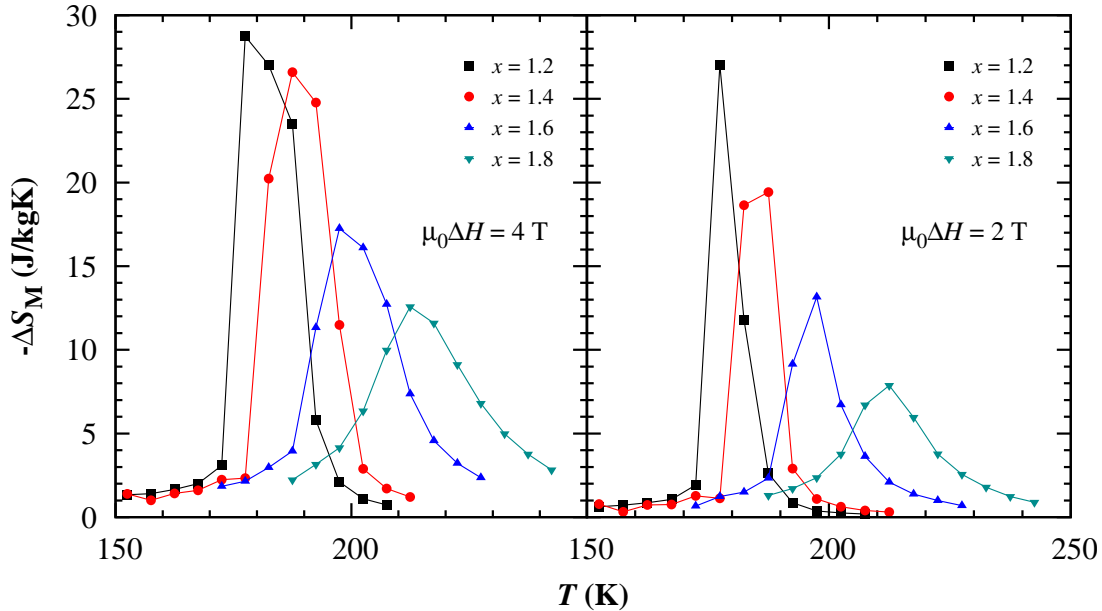


Figure 4.3: Magnetic entropy changes as a function of temperature for all the samples in applied field changes of 0-4 T (left) and 0-2 T (right).

All of the samples display rather large $RCP(\Delta S)$ value due to the large $|\Delta S_M|$ values at the transition – table 4.2. It was suggested that for characterizing magnetocaloric materials it is more convenient to use the specific renormalized cooling power, defined

as $RCP(\Delta S)/\Delta B$ [1]. In the present system, high $RCP(\Delta S)/\Delta B$ values were found. For example, for the compounds with $x = 1.2$ and $x = 1.8$ $RCP(\Delta S)/\Delta B$ values of the order of 109 J/kgT and 69 J/kgT respectively, were obtained. These values are comparable with the results obtained on very good magnetocaloric materials such as pure Gd (111 J/kgT) [58], $\text{La}_{0.7}\text{Pr}_{0.3}\text{Fe}_{11.5}\text{Si}_{1.5}$ (105 J/kgT) [59], $\text{MnFeP}_{0.65}\text{As}_{0.35}$ (82 J/kgT) [60] and $\text{Gd}_5\text{Ge}_{1.8}\text{Si}_{1.8}\text{Sn}_{0.4}$ (31 J/kgT) [61].

Table 4.2: Curie temperatures, maximum entropy changes in external field changes of 0-2 T and 0-4 T respectively, $RCP(\Delta S)$ and $RCP(\Delta S)/\Delta B$ values for $\text{La}_{0.7}\text{Nd}_{0.3}\text{Fe}_{13-x}\text{Si}_x$.

x	T_C (K)	$ \Delta S_M (\text{max})$ (J/kgK)		$RCP(\Delta S)$ (J/kg)		$RCP(\Delta S)/\Delta B$ (J/kgT)	
		0-2T	0-4T	0-2T	0-4T	0-2T	0-4T
		1.2	181	27	28.7	191	435
1.4	188	19.4	26.6	200	423	100	106
1.6	197	13.2	17.2	153	331	76	84
1.8	213	7.9	12.6	136	277	68	69

4.2 Magnetism and Large MCE in $\text{HoFe}_{2-x}\text{Al}_x$ Compounds

One class of materials of interest for magnetocaloric applications are intermetallic compounds containing rare earths, more specifically, the RM_2 Laves phase compounds, where R is a rare earth and M is either a nonmagnetic metal such as Al, or a $3d$ transition metal element such as Fe, Co or Ni. HoAl_2 has a reported Curie temperature around 30 K, having high magnetocaloric properties, however, its $\Delta S_M(T)$ and $\Delta T_{\text{ad}}(T)$ curves are rather narrow [62–64]. HoFe_2 was reported to be ferrimagnetically ordered, the rare earth moments being aligned anti-parallel to the Fe moments [65]. Even though HoAl_2 has rather high magnetocaloric properties, its low Curie temperature makes it unsuitable for room-temperature applications. One way in which we could solve this problem is by combining the high Curie temperature of HoFe_2 with the high magnetocaloric properties of HoAl_2 . Therefore, we can expect that $\text{HoFe}_{2-x}\text{Al}_x$ compounds with properly selected Al concentrations will maintain the high magnetocaloric properties of HoAl_2 while having Curie temperatures close to 300 K. In this section we report on the experimental and theoretical structural, magnetic and magnetocaloric properties of some Fe-rich ($0.36 \leq x \leq 0.4$) and intermediate-region ($0.75 \leq x \leq 1.125$) $\text{HoFe}_{2-x}\text{Al}_x$ intermetallic compounds. The samples were investigated using X-ray diffraction and magnetic measurements. Electronic structure calculations were also performed using the KKR method to support the experimental observations

The compounds with $0.36 \leq x \leq 0.4$ were found to crystallize in the cubic C15 structure, while for the ones with $0.75 \leq x \leq 1.125$ we observed the hexagonal C14 structure. The lattice parameters were found to increase with Al content - table 4.3. These results are in agreement with previously reported data [66–69]. A very small peak

Table 4.3: Lattice parameters for $\text{HoFe}_{2-x}\text{Al}_x$.

x	Structure type	a (Å)	c (Å)
0.36	C15	7.38	7.38
0.375		7.39	7.39
0.4		7.40	7.40
0.75	C14	5.30	8.65
0.875		5.33	8.68
1		5.36	8.70
1.125		5.40	8.75

corresponding to holmium oxide was found in the diffraction patterns due to grinding. For the hexagonal compounds, it was reported that partial order or disorder can occur on the $6h$ or $2a$ sites between Fe and Al [69].

The T_C values were found to decrease linearly with Al content for the hexagonal compounds, while for the cubic samples, Curie temperatures remain roughly unchanged

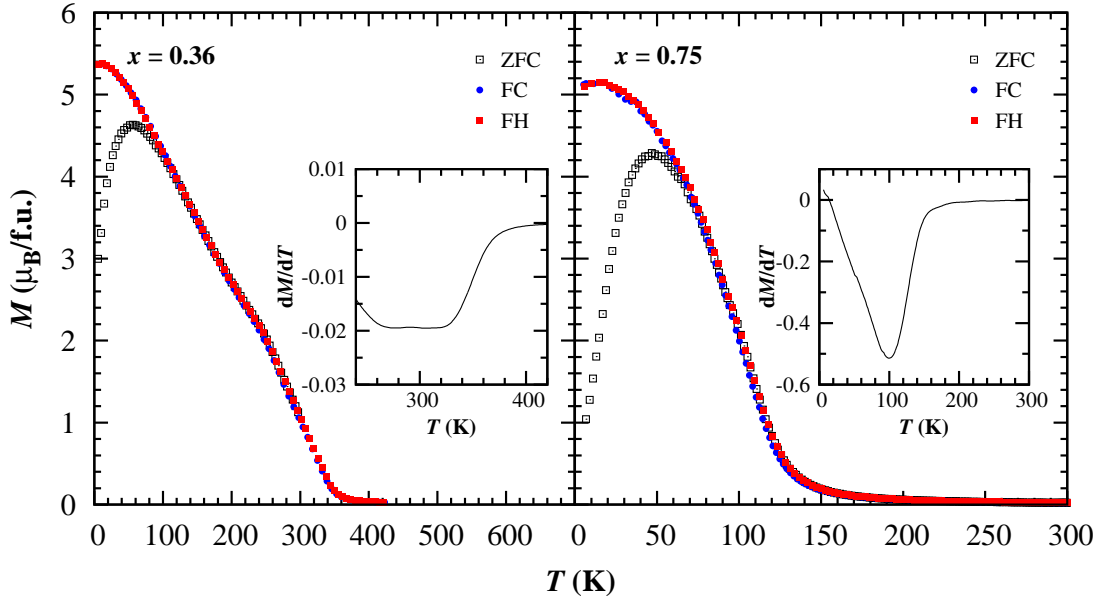


Figure 4.4: Temperature dependences of the magnetizations measured in zero-field cooling (ZFC), field cooling (FC) and field heating (FH) regimes in a low magnetic field of 0.2 T, for the samples with $x = 0.36$ and 0.75. The insets represent the derivative of the magnetization versus temperature.

and close to 300 K – table 4.5. In the cubic compounds, the $3d-3d$ interaction is dominant, leading to high Curie temperatures which decrease with Al content due to an increase in the Fe-Fe distance [66]. In the hexagonal samples, all three of the exchange mechanisms are present: $3d-3d$, $4f-4f$ and $4f-3d$, however, the $4f-4f$ RKKY-type exchange interaction becomes important, leading to rather low Curie temperatures [66]. These compounds show different behaviours in the ZFC and FC regimes. The temperature dependences of the magnetizations exhibited in the ZFC regime point to a spin glass-type behavior in these compounds possibly due to the presence of partial magnetic disorder. However, further investigations into this behavior are required.

It was previously reported that R - M compounds are ferrimagnetically ordered if R is a heavy rare earth [3]. Because Ho is a heavy rare earth, we assumed that in the investigated compounds the Fe and Ho moments are antiparalelly oriented. The magnetic moments per Fe atom have been determined from experimental data by considering the Ho magnetic moment equal to that obtained from neutron diffraction data on HoFe_2 , i.e. $9.15 \mu_{\text{B}}/\text{atom}$ [70]. For the Fe-rich samples, the measured saturation moments at

Table 4.4: Calculated and measured saturation magnetization values and Fe moments at 5 K, along with the calculated Ho moments for $\text{HoFe}_{2-x}\text{Al}_x$.

x	M_{Sat} ($\mu_{\text{B}}/\text{f.u.}$)		M_{Fe} ($\mu_{\text{B}}/\text{atom}$)		M_{Ho} ($\mu_{\text{B}}/\text{atom}$)
	calculated	experiment	calculated	experiment	calculated
0	6.0	6.00 ^a 6.54 ^c	1.73	1.7 ^b 1.88 ^b	9.46
0.36	6.43	7.03	1.77	1.29	9.30
0.375	-	7.06	-	1.28	-
0.4	-	7.21	-	1.21	-
0.75	6.68	7.83	1.96	1.06	9.08
0.875	-	7.75	-	1.24	-
1	7.06	7.70	2.05	1.45	9.07
1.125	7.27	7.60	2.08	1.77	9.04
2	-	9.25 ^c	-	-	-

^a [71]; ^b [72]; ^c [64];

5 K show a slight increase with Al content. For the intermediate-range compounds, the opposite tendency was observed, possibly due to a canted orientation of the Ho moments. The presented behaviour is consistent with data published previously by [66]. The calculated Ho moments show a decrease with Al content, a fact which was attributed to crystal field effects [73]. The calculated Fe magnetic moments increase with Al content for both

cubic and hexagonal samples. This behaviour is correlated with the volume expansion of the unit cell, which is increasing the ASA radii of the Fe atoms as the Al content increases in the samples. For the cubic compounds, the measured Fe moments at 5 K decrease with Al content, probably due to the depletion of the iron 3d bands [66]. For the hexagonal compounds, these values are rather large and increase with Al concentration. These results are consistent with previously reported data [66].

No magnetic hysteresis was found around the Curie temperature in external applied fields up to 4 T for all of the samples, a fact which is important for magnetic refrigeration.

All of the sample were found to undergo a second-order magnetic phase transition at the Curie temperature – figure 4.5. The $\Delta S_M(T)$ peaks are broad and have a symmetrical

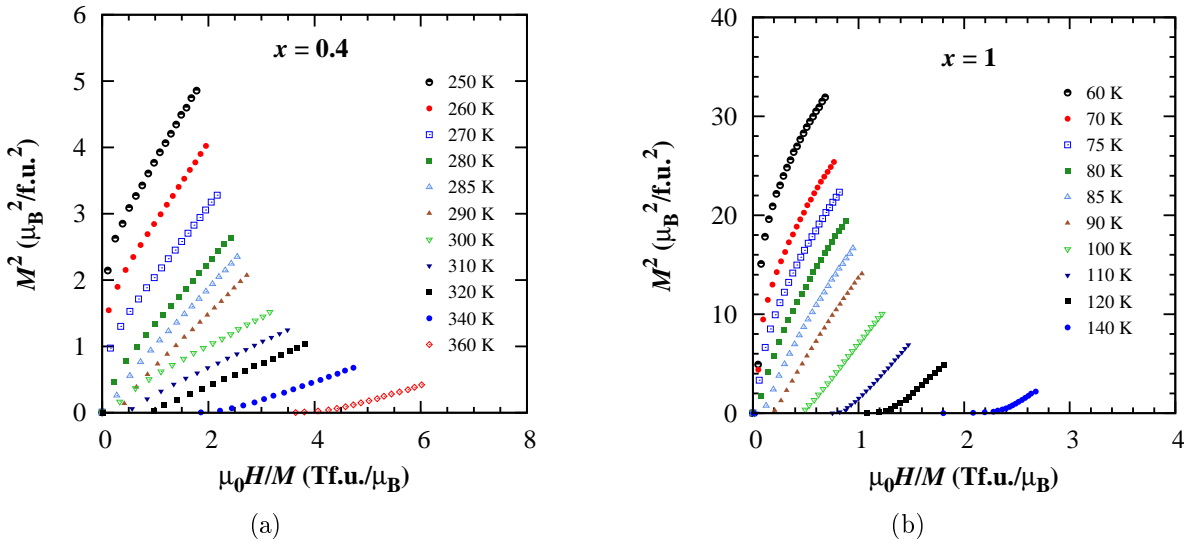


Figure 4.5: Magnetization isotherms and Arrot plots measured around the transition temperatures for the samples with $x = 0.4$ (a) and $x = 1$ (b).

shape, a behavior which is characteristic for materials exhibiting a second-order magnetic phase transition [39] – figure 4.6. For a magnetic field change from 0 to 4 T, the obtained maximum entropy change values increase from 1.73 J/kgK for $x = 0.36$ to 1.82 J/kgK for $x = 0.4$ for the cubic compounds and from 5.1 J/kgK ($x = 0.75$) to 7.6 J/kgK for ($x = 1.125$) for the hexagonal ones – table 4.5.

In the present system, high $RCP(\Delta S)$ values were found due to the large δT_{FWHM} values of the cubic samples and the high $|\Delta S_M|$ values of the hexagonal ones. Also, the $RCP(\Delta S)/\Delta B$ values do not show a significant variation with Al concentration, which is important for magnetic refrigeration. However, from an application point of view, a different way of calculating the useful RCP value was proposed, i.e. the maximal area of the product $\Delta S \times (T_{\text{hot}} - T_{\text{cold}})$, where T_{hot} and T_{cold} are the hot and cold working temperatures, respectively [74]. If we consider the typical working temperature range of room-temperature magnetic refrigerators (270 – 320 K) [74], then the useful RCP values

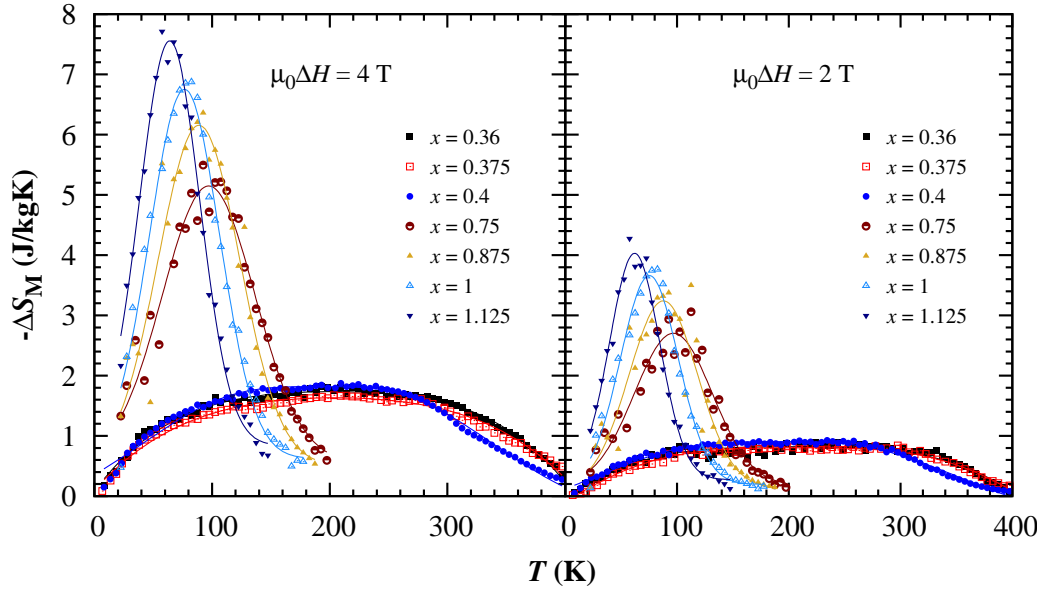


Figure 4.6: Magnetic entropy changes in applied field changes 0-2 T and 0-4 T respectively for all of the investigated samples.

of the cubic samples are greatly reduced. Also, the $|\Delta S_M|$ values of the cubic samples are very low in an applied field change from 0 to 2 T. If we take into account the fact that the price of Ho is much higher than that of Gd, which is being replaced by cheaper materials with better magnetocaloric properties [74], then the possible applications of the cubic $\text{HoFe}_{2-x}\text{Al}_x$ compounds in magnetic refrigerators are very limited. The $|\Delta S_M|$

Table 4.5: Curie temperatures, maximum magnetic entropy changes in external magnetic fields of 0-2 T respectively 0-4 T, $RCP(\Delta S)$ and $RCP(\Delta S)/\Delta B$ values for the investigated $\text{HoFe}_{2-x}\text{Al}_x$ compounds.

x	T_C (K)	$ \Delta S_M (\text{max})$ (J/kgK)		δT_{FWHM} (K)		$RCP(\Delta S)$ (J/kg)		$RCP(\Delta S)/\Delta B$ (J/kgT)	
		0-2T	0-4T	0-2T	0-4T	0-2T	0-4T	0-2T	0-4T
		0.36	295	0.82	1.73	323	330	265	571
0.375	295	0.80	1.63	316	323	253	527	127	132
0.4	283	0.90	1.82	291	292	262	531	131	133
0.75	99	2.7	5.1	82	93	221	474	110	119
0.875	92	3.2	6.2	72	82	230	508	115	127
1	79	3.7	6.8	61	70	226	476	113	119
1.125	64	4	7.6	53	60	212	456	106	114

values of the hexagonal samples are comparable to the ones found for materials with high magnetocaloric properties having transition temperatures in the intermediate range [2]. Furthermore, if we look at the δT_{FWHM} values for $\mu_0\Delta H = 2$ T, we can see that they are

narrow enough so that we could consider the calculated RCP values in table 4.5 equivalent to the useful values described above. If we also consider the lower price of Fe compared to Co (a strategic material), then these compounds could be considered as candidates for magnetic refrigeration applications in the intermediate-temperature range.

4.3 Magnetic Behaviour of Fe in $\text{Er}_{1-x}\text{Zr}_x\text{Fe}_2$ Compounds

The class of intermetallic compounds between rare earth elements (R) and 3d transition metal elements (M) have been widely studied due to the interplay between the localized magnetism of the rare earth and the itinerant magnetism of the transition metal, which leads to a wide variety of magnetic structures [4]. The magnetic properties of $\text{Tb}_{1-x}\text{Zr}_x\text{Fe}_2$ compounds were studied by Tetean et al. [75], in a composition range of $x \leq 0.5$. These compounds were reported to be ferrimagnetically ordered, with Curie temperatures decreasing with Zr content [75]. ErFe_2 was reported to be ferrimagnetically ordered, the Er and Fe moments being antiparallely oriented. Neutron diffraction studies showed that the magnetic contributions of Er and Fe are $M_{\text{Er}} = 8.47 \mu_{\text{B}}$ and $M_{\text{Fe}} = 1.97 \mu_{\text{B}}$ [76]. It was reported that ZrFe_2 compounds show a smaller iron moment of $1.55 \mu_{\text{B}}$ and a lower Curie temperature of 586 K compared to ErFe_2 [77]. ErFe_2 has a reported Curie temperature of 610 K [78] and a compensation point at 490 K [79]. The $\Delta T_{\text{ad}}(T)$ curve for ErFe_2 has a form analogous to that observed in gadolinium iron garnet: with increasing temperature, the MCE suddenly changes its sign from positive to negative near T_{K} [2, 79]. In the following section, We report on the theoretical and experimental structural, magnetic and magnetocaloric properties of $\text{Er}_{1-x}\text{Zr}_x\text{Fe}_2$ compounds in the composition range $0.1 \leq x \leq 0.4$. We performed X-Ray diffraction, magnetic and magnetic susceptibility measurements. Electronic structure calculations were performed using the KKR and LMTO+U methods in order to support the experimental observations.

X-Ray diffraction results showed that all of the investigated samples crystallize in the cubic MgCu_2 (C15) structure, where the Er/Zr and Fe atoms occupy the $8a$ and $16d$ sites respectively. Small amounts of erbium oxide and zirconium oxide were found in the XRD

Table 4.6: Lattice parameters for $\text{Er}_{1-x}\text{Zr}_x\text{Fe}_2$.

x	a (\AA)
0	7.28 ^a
0.1	7.25
0.2	7.23
0.3	7.21
0.4	7.17

^a [78]

patterns due to grinding. The lattice parameters decrease slowly with Zr content – table 4.6 – due to the smaller ionic radius of Zr^{4+} compared to Er^{3+} .

All of the investigated samples present a compensation point – figure 4.7. The Curie temperatures were found to increase with Zr content, while the compensation temperatures decrease when Zr concentration increases – table 4.7. The Curie temperatures in

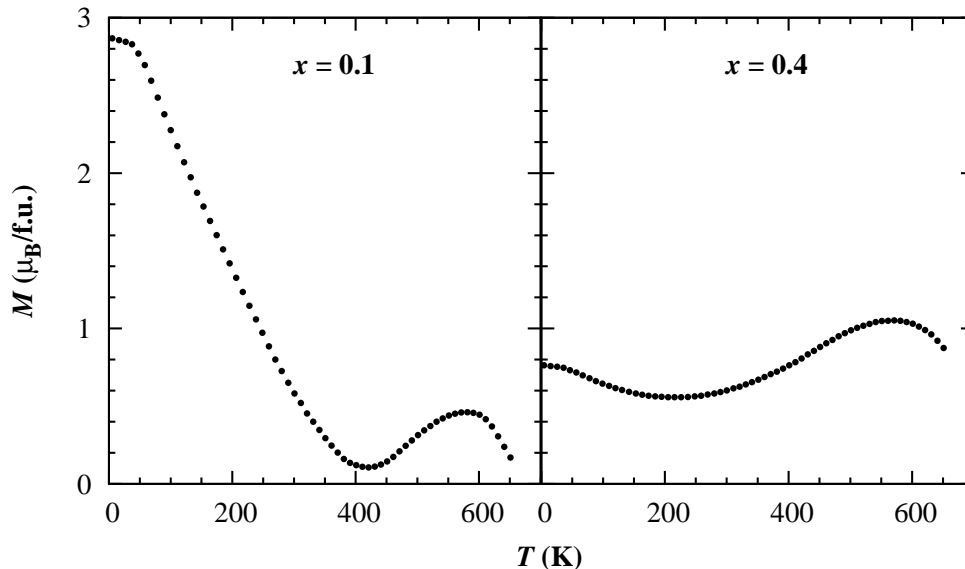


Figure 4.7: Magnetization versus temperature plots for the samples with $x = 0.1$ and $x = 0.4$ measured in a small field of 0.2 T.

these compounds are mainly determined by the Fe-Fe interactions. In our samples, the shrinkage of the lattice parameter causes an increase of the overlap of the $3d$ orbitals, increasing the Curie temperature. The decrease of the compensation temperatures with Zr concentration could be explained by a weakening of the $4f$ - $4f$ interaction when Er is replaced by Zr. The calculated Fe moments vary only slightly with Zr content, possibly due to band-filling effects when Zr is added. The KKR calculations show no changes in both the spin and orbital contributions of Er when Zr concentration increases, however,

Table 4.7: Curie and compensation temperatures, saturation moments and Fe moments at 5 K for $\text{Er}_{1-x}\text{Zr}_x\text{Fe}_2$ compounds.

x	T_C (K)	T_K (K)	M_S (μ_B /f.u.)	M_{Fe} (μ_B /atom)
0	610 ^a	490 ^b	4.53 ^c	1.97 ^c
0.1	630	397	4.23	1.70
0.2	637	351	3.55	1.61
0.3	658	321	2.62	1.65
0.4	684	220	1.98	1.55

^a [78]; ^b [79]; ^c Measured at 4.2 K [76].

when the U correction is added, the spin moment of Er shows a decrease with Zr content, probably to the weakening of the $4f$ - $4f$ interaction. A polarization of the $4d$ band of Zr was found and its value is given in table 4.8. The saturation moments at 5 K decrease

Table 4.8: Calculated saturation magnetization values and Fe, Ho and Zr magnetic moments for $\text{Er}_{1-x}\text{Zr}_x\text{Fe}_2$. The values $U = 8$ eV and $J = 0.9$ eV were used in the LSDA+U calculations.

	M_{Er} ($\mu_{\text{B}}/\text{atom}$)			M_{Fe} ($\mu_{\text{B}}/\text{atom}$)			M_{Zr} ($\mu_{\text{B}}/\text{atom}$)			M_{S} ($\mu_{\text{B}}/\text{f.u.}$)
	Spin	Orbit	Total	Spin	Orbit	Total	Spin	Orbit	Total	
KKR (LSDA)										
ErFe_2	2.890	5.120	8.010	-1.580	-0.068	-1.648	-	-	-	4.714
$\text{Er}_{0.9}\text{Zr}_{0.1}\text{Fe}_2$	2.890	5.110	8.000	-1.617	-0.065	-1.682	0.620	0.010	0.630	3.899
$\text{Er}_{0.8}\text{Zr}_{0.2}\text{Fe}_2$	2.890	5.110	8.000	-1.620	-0.064	-1.684	0.590	0.010	0.600	3.152
LMTO (LSDA+U)										
ErFe_2	3.444	-	3.444	-1.641	-	-1.641	-	-	-	0.162
$\text{Er}_{0.625}\text{Zr}_{0.375}\text{Fe}_2$	3.162	-	3.162	-1.632	-	-1.632	0.591	-	0.591	-1.066

with Zr content, a behaviour which is consistent with ferrimagnetic order. We have to note that the magnetization value at the compensation point increases with Zr content – figure 4.8. This leads us to believe that there is a possible rotation of the Er moments in these compounds when Zr content increases. Considering the Er moment the same as the one determined from neutron diffraction data in ErFe_2 , i.e. $8.47 \mu_{\text{B}}$ [76], the Fe magnetic moments were determined. The Fe moments at 5 K show a strong dependence

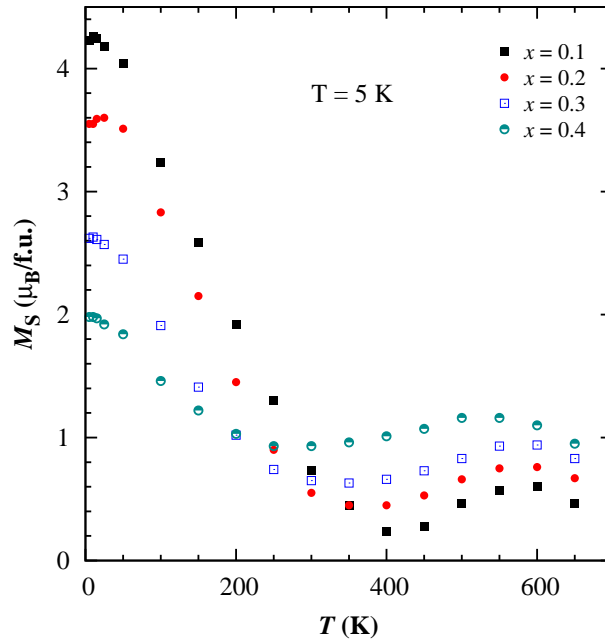


Figure 4.8: Temperature dependences of the spontaneous magnetizations.

on Zr content, possibly due to a filling of the $3d$ band when Zr is added. However, if we take into account the possible decrease and rotation of the Er moments when Zr is added, along with the slight variation of the Fe moments shown by band structure calculations and previously published data [75], then it is possible that the strong decrease of the measured Fe moments in these compounds is not a real one. Further investigations are required in order to fully explain this behaviour.

The magnetocaloric effect was also studied. All of the investigated samples display rather wide $\Delta S_M(T)$ curves with a plateau which decreases in width when Zr concentration increases – figure 4.9. These compounds display rather low $|\Delta S_M|$ values – table 4.9. The

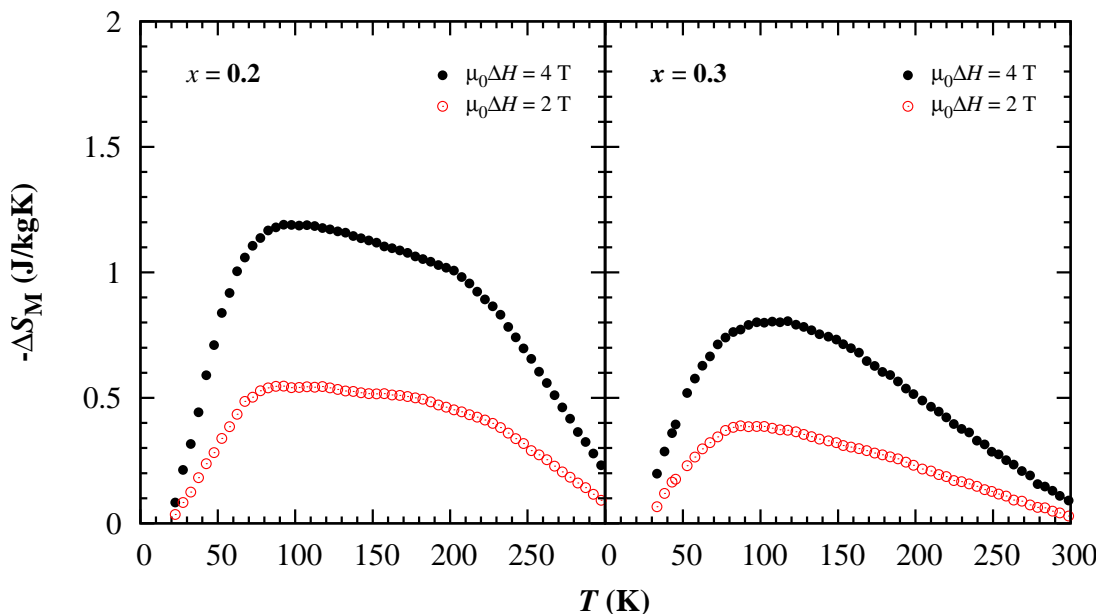


Figure 4.9: Magnetic entropy changes versus temperature plots in external applied field changes of 0-2 T and 0-4 T respectively for the samples with $x = 0.2$ and $x = 0.3$.

$RCP(\Delta S)$ values are rather large and decrease with Zr content from 318 J/kg for $x = 0.1$ to 70 J/kg for $x = 0.4$ in an applied field change of 0-4 T. The large $RCP(\Delta S)$ values obtained for these compounds are mainly due to the large δT_{FWHM} values of the $\Delta S_M(T)$ curves. It is worthwhile to note that $RCP(\Delta S)/\Delta B$ values do not show a significant variation with Zr content between applied field changes of 0-2 T and 0-4 T respectively.

From an application point of view, even though these compounds display rather large $RCP(\Delta S)$ values and compensation points close to room temperature, this is not sufficient to consider them for magnetocaloric applications. The low maximum values of the magnetic entropy changes and the fact that close to the compensation point $|\Delta S_M|$ values are close to zero make these materials unsuitable for magnetic refrigeration applications.

Table 4.9: Maximum magnetic entropy changes in external magnetic fields of 0-2 T respectively 0-4 T, $RCP(\Delta S)$ and $RCP(\Delta S)/\Delta B$ values for the investigated $Er_{1-x}Zr_xFe_2$ compounds.

x	$ \Delta S_M (\text{max})$ (J/kgK)		δT_{FWHM} (K)		$RCP(\Delta S)$ (J/kg)		$RCP(\Delta S)/\Delta B$ (J/kgT)	
	0-2T	0-4T	0-2T	0-4T	0-2T	0-4T	0-2T	0-4T
0.1	0.55	1.19	252	267	139	318	70	80
0.2	0.54	1.17	210	215	113	252	57	63
0.3	0.38	0.81	175	177	67	144	34	36
0.4	0.21	0.50	131	140	28	70	14	18

Chapter 5

Magnetic Properties of Rare Earth - 3d Transition Metal Oxides

5.1 Magnetic Properties and MCE in $La_{1.4-x}Ce_xCa_{1.6}Mn_2O_7$ Perovskites Synthesized Through the Sol-Gel Method

During the last two decades, many investigations on the magnetic and transport properties of the so called double layered perovskites with the chemical composition $R_{2-2x}A_{1+2x}Mn_2O_7$ were reported [80–89], where R is a trivalent rare earth cation like La, Nd, or Pr and A is a divalent alkaline earth cation like Sr, Ca or Ba. The physical properties of these materials are sensitive to small changes in composition due to their layered structure [83]. These compounds exhibit a colossal magnetoresistance (CMR) effect at low temperatures [90–92] and large magnetic entropy change (ΔS_M) values for moderate magnetic field changes [93–98]. In this section, the effect of Ce doping on the physical properties of $La_{1.4}Ca_{1.6}Mn_2O_7$ double layered manganites was investigated using X-Ray diffraction, X-Ray photoelectron spectroscopy, magnetic and magnetic susceptibility measurements.

The X-ray diffraction analysis showed that the polycrystalline samples are single phase with a $Sr_3Ti_2O_7$ -type tetragonal structure. The smaller lattice parameters determined for $La_{1.2}Ce_{0.2}Ca_{1.6}Mn_2O_7$ can be explained due to the smaller ionic radius of Ce compared to La – table 5.1. The slight decrease of the c/a ratio suggests that the lattice contracts, preferably in the c -direction rather than in the a -direction.

In order to observe the effect of Ce substitution, the temperature dependences of

Table 5.1: Lattice parameters, c/a ratios and crystallite sizes estimated from XRD patterns for $\text{La}_{1.4-x}\text{Ce}_x\text{Ca}_{1.6}\text{Mn}_2\text{O}_7$.

x	a (Å)	c (Å)	a/c	Crystallite size (nm)
0	3.845(7)	19.156(7)	4.982	25
0.2	3.842(5)	19.098(7)	4.970	17

the magnetizations in zero field cooling (ZFC) and field cooling (FC) modes in an applied magnetic field of 0.2 T were recorded. The curves presented in figure 5.1 show a change in slope in the 50-200 K temperature range. The Curie temperature decreases

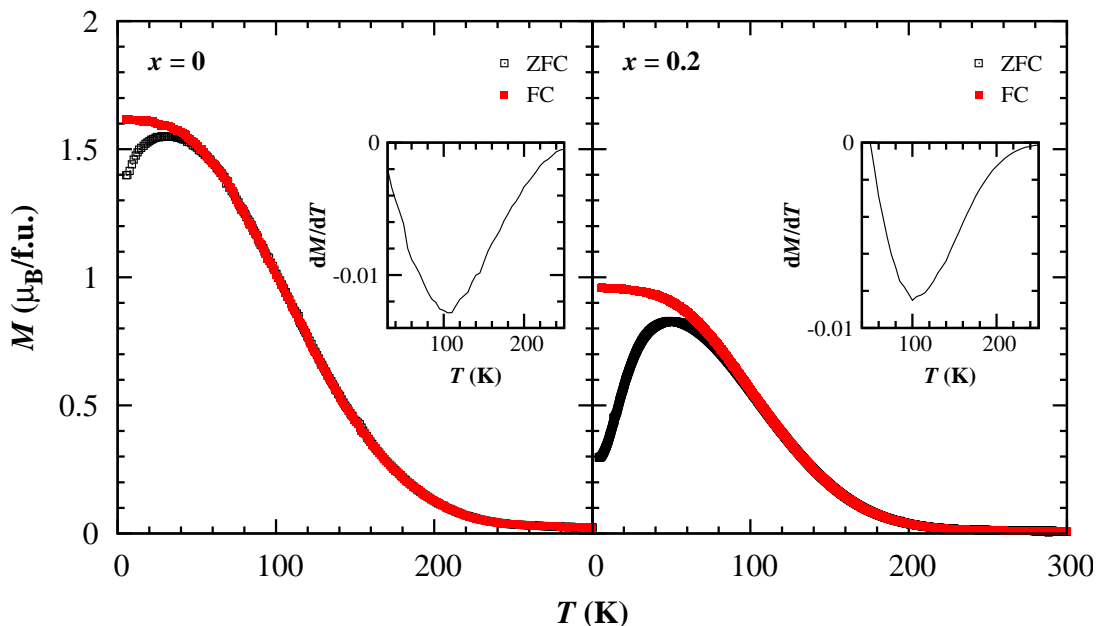


Figure 5.1: Temperature dependences of the magnetizations measured in an applied field of 0.2 T in zero-field cooled (ZFC) and field cooled (FC) regimes for $\text{La}_{1.4}\text{Ca}_{1.6}\text{Mn}_2\text{O}_7$ (left) and $\text{La}_{1.2}\text{Ce}_{0.2}\text{Ca}_{1.6}\text{Mn}_2\text{O}_7$ (right). The insets represent the derivative of the magnetizations versus temperature.

from around 109 K to 100 K when La is partially substituted by Ce. This can be correlated with the distortion of the Mn-O-Mn angle which weakens the exchange interaction. There are clear differences between the ZFC and FC curves at temperatures below 50 K for $\text{La}_{1.4}\text{Ca}_{1.6}\text{Mn}_2\text{O}_7$ and 75 K for $\text{La}_{1.2}\text{Ce}_{0.2}\text{Ca}_{1.6}\text{Mn}_2\text{O}_7$. This spin glass-like behavior could be attributed to frustration due to random competing ferromagnetic double exchange, super-exchange and antiferromagnetic interactions, together with the anisotropy originating from the layered structure.

The magnetization of the two samples does not saturate even in magnetic fields up to 12 T at 5 K – figure 5.2 – which can be explained by the absence of true long-range ferromagnetic order due to the small grain size of the two samples [99]. When the field

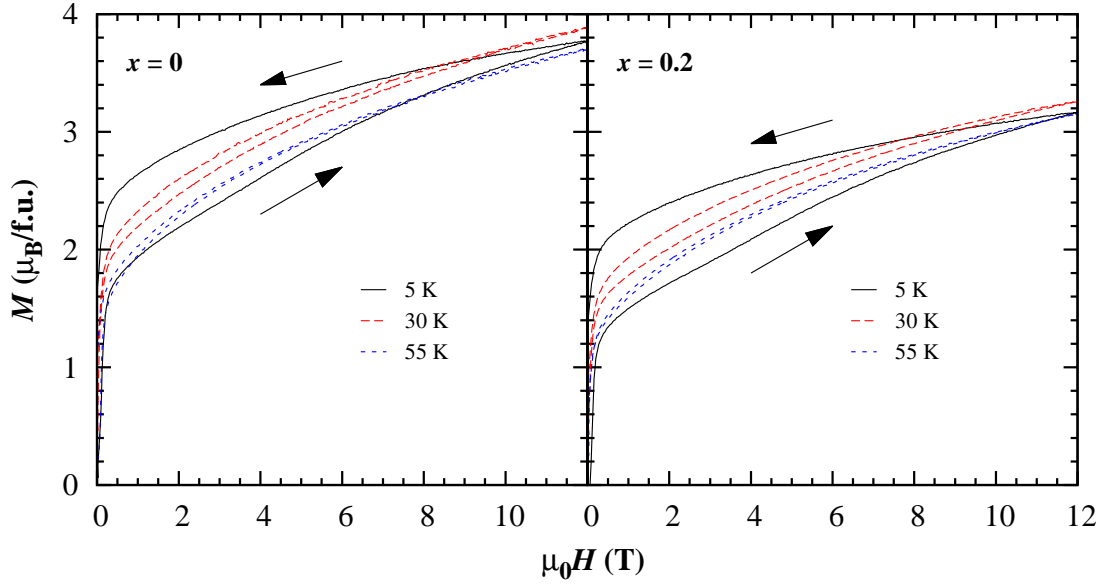


Figure 5.2: Magnetic field dependence of the magnetizations at selected temperatures in applied fields up to 12 T for $\text{La}_{1.4-x}\text{Ce}_x\text{Ca}_{1.6}\text{Mn}_2\text{O}_7$ manganites.

was ramped up, the magnetization was even higher at 30 K than at 5 K, indicating that the system is phase-separated containing FM and AFM clusters. The coexistence of these two states leads to frustration, and thus to a spin glass-like behavior. The $M(H)$ curves exhibit clear hysteresis at 5 K, which diminishes with increasing temperature and is almost absent at 55 K – figure 5.2.

The Ce-doped compound undergoes a second-order magnetic phase transition from a ferromagnetic to a paramagnetic state at T_C – figure 5.3. The same behaviour was found

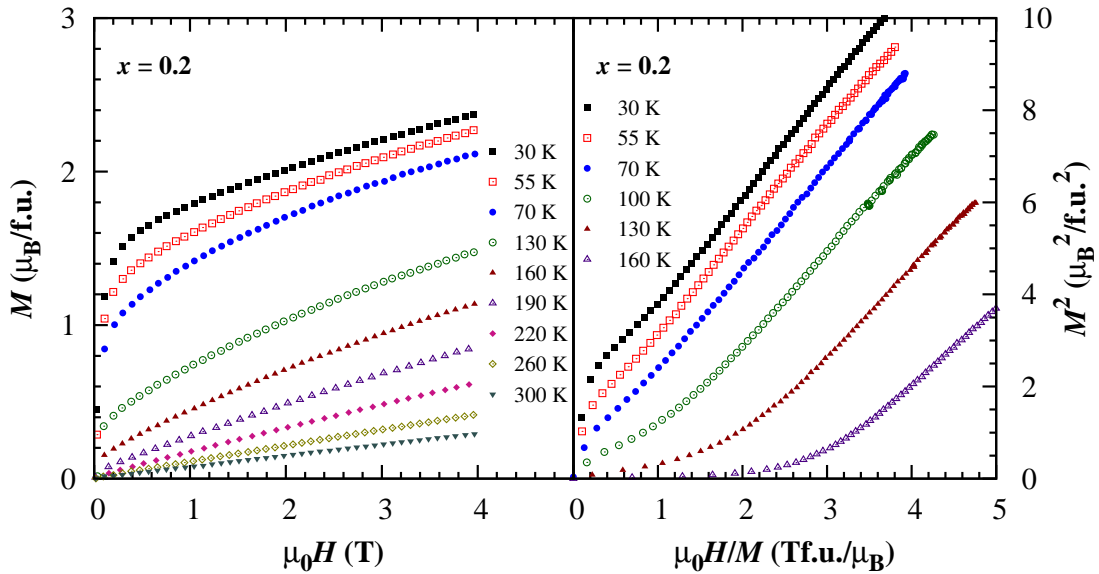


Figure 5.3: Magnetization isotherms measured around the transition temperature in applied fields of up to 4 T and Arrott plots for $\text{La}_{1.2}\text{Ce}_{0.2}\text{Ca}_{1.6}\text{Mn}_2\text{O}_7$.

for the undoped sample.

The temperature dependence of the reciprocal susceptibility recorded above room temperature for the Ce-doped sample is shown in figure 5.4. The deviation of the

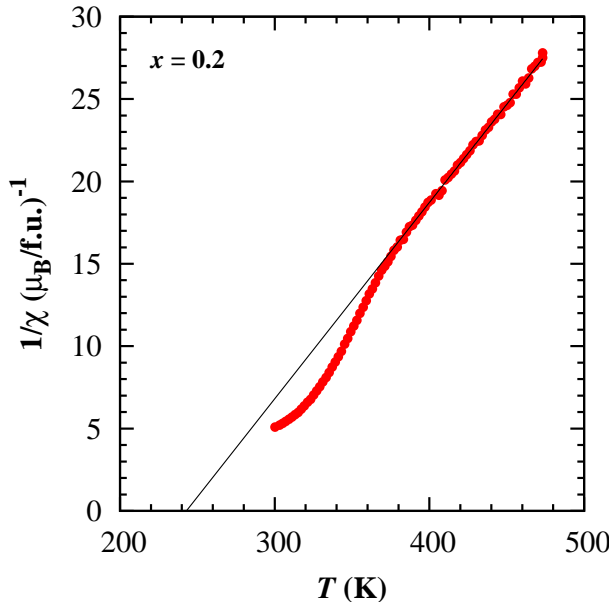


Figure 5.4: Temperature dependence of the reciprocal susceptibility for $\text{La}_{1.2}\text{Ce}_{0.2}\text{Ca}_{1.6}\text{Mn}_2\text{O}_7$.

experimental points from linearity and the decreased value of the magnetization for $\text{La}_{1.2}\text{Ce}_{0.2}\text{Ca}_{1.6}\text{Mn}_2\text{O}_7$ suggest an antiferromagnetic alignment of the Ce and Mn moments. Previous results on similar compounds revealed that at temperatures below 100 K the Ce moments are ordered antiferromagnetically with respect to the ferromagnetic Mn moments and thus form a ferrimagnetic ground state. In the 400-500 K temperature range the magnetic susceptibility of $\text{La}_{1.2}\text{Ce}_{0.2}\text{Ca}_{1.6}\text{Mn}_2\text{O}_7$ follows a Curie-Weiss law with a paramagnetic Curie temperature of about 243 K and an effective magnetic moment of $6.1 \mu_{\text{B}}/\text{f.u.}$. Considering the small contribution of the Ce ions to the effective magnetic moment ($2.54 \mu_{\text{B}}/\text{atom}$), we calculated an effective magnetic moment of about $4.25 \mu_{\text{B}}$ for the Mn atoms, which indicates the presence of both Mn^{4+} and Mn^{3+} ions in $\text{La}_{1.2}\text{Ce}_{0.2}\text{Ca}_{1.6}\text{Mn}_2\text{O}_7$.

In order to investigate the valency of the Ce and Mn ions, the XPS spectra of the Ce 3d and Mn 3s core levels in $\text{La}_{1.2}\text{Ce}_{0.2}\text{Ca}_{1.6}\text{Mn}_2\text{O}_7$ were recorded. As shown in figure 5.5(a), both Ce^{3+} and Ce^{4+} ions are present in the sample and show a spin-orbit splitting of 18.3 eV. An estimation of the $\text{Ce}^{3+}/\text{Ce}^{4+}$ ratio is very difficult due to the presence of the Mn $L_3M_{23}M_{45}$ Auger line at 900 eV. The Mn 3s core level spectrum – figure 5.5(b) – shows an exchange splitting of about 4.7 eV. In manganites, the magnitude of the Mn 3s core level splitting allows the estimation of the Mn formal valence [33]. For $\text{La}_{1.2}\text{Ce}_{0.2}\text{Ca}_{1.6}\text{Mn}_2\text{O}_7$ the estimated value for the Mn valence is 3.7+, corresponding to

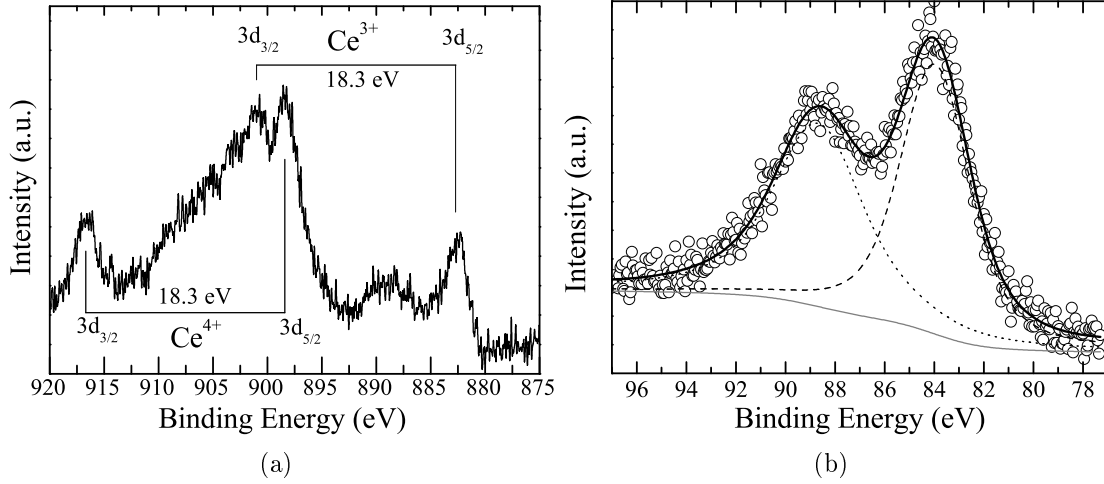


Figure 5.5: XPS spectra of (a) Ce 3d and (b) Mn 3s core levels in $\text{La}_{1.2}\text{Ce}_{0.2}\text{Ca}_{1.6}\text{Mn}_2\text{O}_7$.

an effective magnetic moment of about $4.2 \mu_B$, in excellent agreement with the results obtained from magnetization data.

The magnetocaloric effect was also investigated. The maximum $|\Delta S_M|$ values were obtained for temperatures very close to the magnetic transition ones and the peaks are nearly symmetrical around their maximum values, a characteristic for second-order magnetic transition materials [100]. The maximum values of $|\Delta S_M|$ are rather small, but the

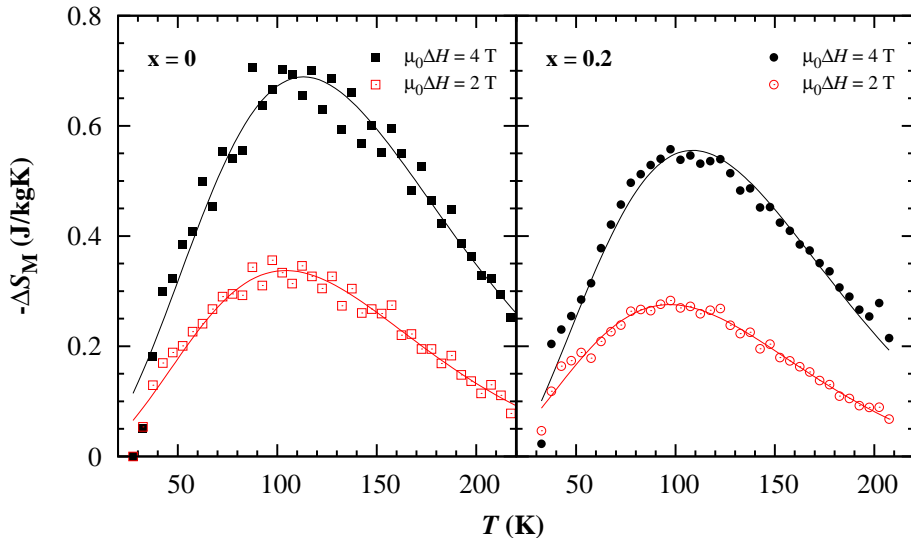


Figure 5.6: Magnetic entropy changes for $\text{La}_{1.4-x}\text{Ce}_x\text{Ca}_{1.6}\text{Mn}_2\text{O}_7$ manganites in applied field changes of 0-2 T and 0-4 T respectively.

magnetic entropy change has a significant value over a broad temperature range. The $|\Delta S_M|$ values obtained in an applied field change of 0-4 T decrease 0.71 J/kgK ($x = 0$) and 0.56 J/kgK ($x = 0.2$) respectively. The $RCP(S)$ values also decrease from 102 J/kg

for $x = 0$ to 77 J/kg for $x = 0.2$ respectively for an applied field change of 0-4 T. These values are comparable to those previously obtained for $\text{La}_{1.4-x}\text{Ce}_x\text{Ca}_{1.6}\text{Mn}_2\text{O}_7$ [93, 97–99].

5.2 Effects of the Pr, Nd, Sm and Gd Substitution for La on the Magnetic Properties of $\text{La}_{1.4}\text{Ca}_{1.6}\text{Mn}_2\text{O}_7$

In the past years, many studies have revealed that double layered perovskite manganites $R_{2-2x}A_{1+2x}\text{Mn}_2\text{O}_7$ ($R = \text{La, Nd, Pr etc.}$ and $A = \text{Sr, Ca, or Ba}$) exhibit intriguing properties such as enhanced magnetoresistance, charge ordering, anisotropic transport in charge carriers, large magnetic entropy changes, and the possibility of two types of ferromagnetic ordering [80–92, 101, 102]. Due to their layered structure, the physical properties of these materials are affected by small changes in their composition [83]. These materials also exhibit a large magnetocaloric effect [94–98, 103]. In the following section, we discuss the effects of the partial substitution of Pr, Nd, Sm and Gd for La on the magnetic and magnetocaloric properties of $\text{La}_{1.4}\text{Ca}_{1.6}\text{Mn}_2\text{O}_7$ prepared through a direct sol-gel method. The structural properties were investigated using X-Ray diffraction, while the morphological and compositional characterization was performed using SEM-EDX and TEM. The magnetic properties of these compounds were investigated through magnetic and magnetic susceptibility measurements.

X-ray diffraction results showed that the polycrystalline powders obtained by the sol-gel method are single phase with a $\text{Sr}_3\text{Ti}_2\text{O}_7$ -type tetragonal ($I4/mmm$) structure. The lattice parameters determined for $\text{La}_{1.2}R_{0.2}\text{Ca}_{1.6}\text{Mn}_2\text{O}_7$ ($R = \text{Pr, Nd, Sm and Gd}$) are smaller than those found for $\text{La}_{1.4}\text{Ca}_{1.6}\text{Mn}_2\text{O}_7$ which can be attributed to the smaller ionic radius of Pr^{3+} , Nd^{3+} , Sm^{3+} and Gd^{3+} compared to La^{3+} . The substitution of smaller Pr,

Table 5.2: Lattice parameters, c/a ratio and crystallite sizes estimated from XRD patterns.

Sample	a (Å)	c (Å)	c/a	Crystallite size (nm)
$\text{La}_{1.4}\text{Ca}_{1.6}\text{Mn}_2\text{O}_7$	3.844	19.176	4.988	22
$\text{La}_{1.2}\text{Pr}_{0.2}\text{Ca}_{1.6}\text{Mn}_2\text{O}_7$	3.840	19.165	4.990	26.4
$\text{La}_{1.2}\text{Nd}_{0.2}\text{Ca}_{1.6}\text{Mn}_2\text{O}_7$	3.843	19.154	4.983	24.8
$\text{La}_{1.2}\text{Sm}_{0.2}\text{Ca}_{1.6}\text{Mn}_2\text{O}_7$	3.843	19.126	4.976	24.6
$\text{La}_{1.2}\text{Gd}_{0.2}\text{Ca}_{1.6}\text{Mn}_2\text{O}_7$	3.847	19.193	4.988	21.4

Nd, Sm and Gd ions for larger La ions increases the inter-layer lattice distortion, causing the decrease of the lattice parameters. The values found for the c/a ratios are typical for $\text{La}_{2-2x}\text{Ca}_{1+2x}\text{Mn}_2\text{O}_7$ perovskites [81, 99, 104].

The compositional analysis was performed by energy dispersive x-ray microanalysis (EDX), which indicated that the compositions of the samples were nearly identical to

Table 5.3: Compositions of the investigated samples obtained from the EDX analysis.

Sample	La (at.%)	R (at.%)	Ca (at.%)	Mn (at.%)	O (at.%)
$\text{La}_{1.4}\text{Ca}_{1.6}\text{Mn}_2\text{O}_7$	11.23	-	11.86	18.74	58.17
$\text{La}_{1.2}\text{Pr}_{0.2}\text{Ca}_{1.6}\text{Mn}_2\text{O}_7$	7.22	1.19	8.69	13.41	69.50
$\text{La}_{1.2}\text{Nd}_{0.2}\text{Ca}_{1.6}\text{Mn}_2\text{O}_7$	7.15	1.11	8.65	13.58	69.51
$\text{La}_{1.2}\text{Sm}_{0.2}\text{Ca}_{1.6}\text{Mn}_2\text{O}_7$	7.43	1.11	9.05	13.58	68.83
$\text{La}_{1.2}\text{Gd}_{0.2}\text{Ca}_{1.6}\text{Mn}_2\text{O}_7$	6.75	1.15	8.48	11.01	72.62

the nominal one within the accuracy of EDX – table 5.3. The surface morphology of the samples has been observed with SEM and TEM. Figure 5.7 shows the granular nature of $\text{La}_{1.4}\text{Ca}_{1.6}\text{Mn}_2\text{O}_7$, with grains sizes smaller than 30 nm that tend to agglomerate. Similar

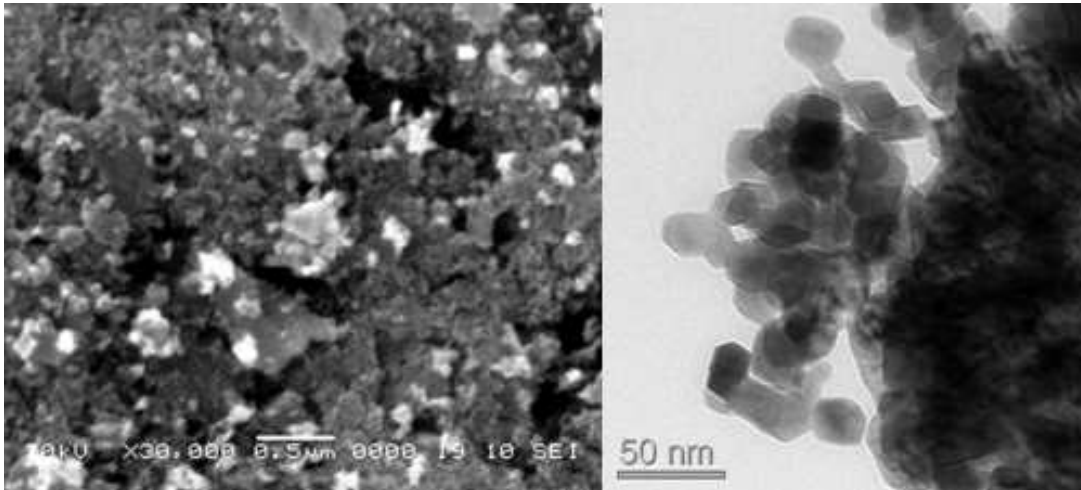


Figure 5.7: SEM (left) and TEM (right) images of $\text{La}_{1.4}\text{Ca}_{1.6}\text{Mn}_2\text{O}_7$.

images were recorded for all samples, indicating that the partial substitution of Pr, Nd, Sm and Gd for La in $\text{La}_{1.4}\text{Ca}_{1.6}\text{Mn}_2\text{O}_7$ does not have a strong influence on the morphology of the samples. The TEM analysis revealed that the obtained $\text{La}_{1.2}\text{R}_{0.2}\text{Ca}_{1.6}\text{Mn}_2\text{O}_7$ with $R = \text{La, Pr, Nd, Sm and Gd}$ powders consist of spherical particles with grain sizes between 20 and 30 nm, in excellent agreement with the crystallite sizes estimate from the XRD patterns. The HRTEM and SAED investigations confirmed the good crystallinity of the grains.

The temperature dependences of the magnetizations in zero field cooling (ZFC) and field cooling (FC) modes measured in an applied field of 0.2 T are presented in figure 5.8. The ZFC and FC magnetizations show a clear splitting at low temperatures and a decrease in the temperature range of 50 – 200 K. Such a wide ferromagnetic transition is a typical feature for double layered $\text{R}_{2-2x}\text{A}_{1+2x}\text{Mn}_2\text{O}_7$ manganites and arises

due to the appearance of short range 2D-magnetic order at temperatures higher than the 3D-ferromagnetic transition temperature [17, 105]. This is supported also by the observation that even at room temperature, the magnetization is not zero, but has values around $0.02 \mu_B/\text{f.u.}$ in 0.2 T for all samples. The Curie temperature of $\text{La}_{1.2}\text{R}_{0.2}\text{Ca}_{1.6}\text{Mn}_2\text{O}_7$ de-

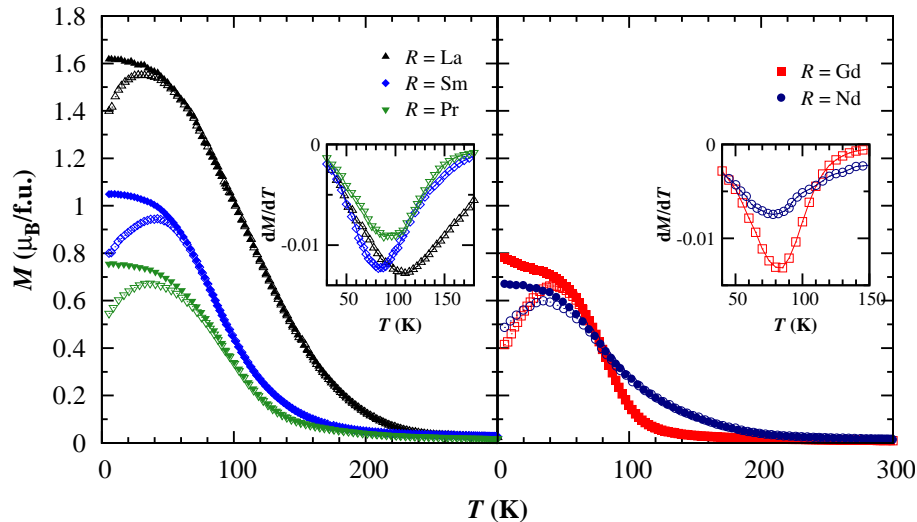


Figure 5.8: Temperature dependences of ZFC (open symbols) and FC (filled symbols) magnetizations in an applied field of 0.2 T for $\text{La}_{1.2}\text{R}_{0.2}\text{Ca}_{1.6}\text{Mn}_2\text{O}_7$. The insets represent the derivative of the magnetizations versus temperature.

creases from around 109 K for $R = \text{La}$ to ~ 92.5 K for $R = \text{Pr}$, ~ 78 K for $R = \text{Nd}$, ~ 85.5 K for $R = \text{Sm}$, and ~ 81.5 K for $R = \text{Gd}$. This behaviour can be correlated with a distortion of the Mn-O-Mn angle which leads to a weakening of the exchange interaction. The clear differences between FC and ZFC data at low temperatures indicate a spin glass-like state. This may be due to frustration of random competing ferromagnetic and

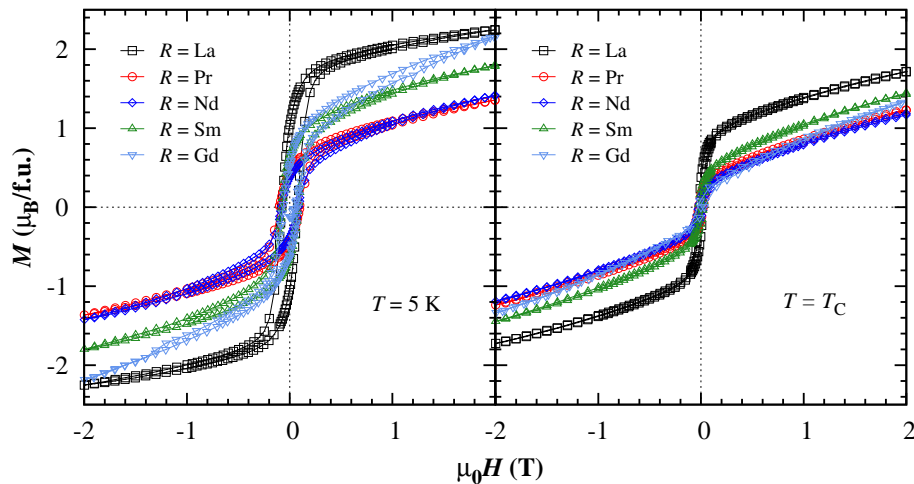


Figure 5.9: Magnetic hysteresis loops for all of the samples measured at 5 K (left) and at the Curie temperature (right).

antiferromagnetic interactions together with the anisotropy originating from the layered structure [106, 107]. The hysteresis effect observed in the low temperature region – figure 5.9 – supports this explanation. The $M(H)$ curves exhibit a clear hysteresis at 5 K, which diminishes with increasing temperature and is almost absent for temperatures close to the Curie temperature.

In the 400-500 K temperature range the magnetic susceptibility of all investigated samples obeys a Curie-Weiss law. The effective magnetic moments for the Mn atoms were calculated considering the contribution of the R^{3+} (Pr, Nd, Sm and Gd) ions to the total effective magnetic moment as $g\sqrt{J(J+1)}$. The values obtained for the effective

Table 5.4: Transition and paramagnetic Curie temperatures and effective magnetic moments for the investigated samples.

Sample	T_C (K)	Θ_p (K)	μ_{eff} ($\mu_B/\text{f.u.}$)	μ_{eff}^R (μ_B/atom)	$\mu_{\text{eff}}^{\text{Mn}}$ (μ_B/atom)
$\text{La}_{1.4}\text{Ca}_{1.6}\text{Mn}_2\text{O}_7$	109	246	5.94	0	4.20
$\text{La}_{1.2}\text{Pr}_{0.2}\text{Ca}_{1.6}\text{Mn}_2\text{O}_7$	92.5	234	6.29	3.58	4.30
$\text{La}_{1.2}\text{Nd}_{0.2}\text{Ca}_{1.6}\text{Mn}_2\text{O}_7$	78	231	6.04	3.62	4.11
$\text{La}_{1.2}\text{Sm}_{0.2}\text{Ca}_{1.6}\text{Mn}_2\text{O}_7$	85.5	248	5.99	0.85	4.23
$\text{La}_{1.2}\text{Gd}_{0.2}\text{Ca}_{1.6}\text{Mn}_2\text{O}_7$	81.5	197	7.31	7.94	4.52

magnetic moments of the Mn atoms indicate the presence of both Mn^{4+} and Mn^{3+} ions in the investigated compounds – table 5.4. These values indicate that the magnetic moment at low temperature for the Mn atoms is around 3.3-3.4 μ_B , which supports the picture of a canted spin arrangement in the investigated double layered manganites.

XPS investigations were also performed. The Mn 3s core level XPS spectra of the investigated manganites showed an exchange splitting around 4.7 eV – table 5.5. In order to obtain the values of the exchange splitting, ΔE_{ex} , the spectra were fitted using two components after the subtraction of a Shirley-type background [108]. The Mn formal

Table 5.5: Fitting parameters for Mn 3s XPS spectra of investigated samples, the exchange splitting ΔE_{ex} , the estimated Mn valence and the calculated effective magnetic moments.

Sample	Binding Energy (eV)		ΔE_{ex} (eV)	Mn valence	$\mu_{\text{eff}}^{\text{Mn}}$ (μ_B/atom)
	Component 1	Component 2			
$\text{La}_{1.4}\text{Ca}_{1.6}\text{Mn}_2\text{O}_7$	83.62	88.35	4.73	3.66+	4.25
$\text{La}_{1.2}\text{Pr}_{0.2}\text{Ca}_{1.6}\text{Mn}_2\text{O}_7$	83.72	88.45	4.74	3.65+	4.26
$\text{La}_{1.2}\text{Nd}_{0.2}\text{Ca}_{1.6}\text{Mn}_2\text{O}_7$	83.96	88.68	4.72	3.67+	4.24
$\text{La}_{1.2}\text{Sm}_{0.2}\text{Ca}_{1.6}\text{Mn}_2\text{O}_7$	83.99	88.76	4.77	3.61+	4.30
$\text{La}_{1.2}\text{Gd}_{0.2}\text{Ca}_{1.6}\text{Mn}_2\text{O}_7$	84.11	88.74	4.63	3.79+	4.06

valence was calculated from the ΔE_{ex} values by means of equation (3.1). The results are in excellent agreement with magnetic data.

The magnetocaloric properties of these compounds were also investigated. The magnetic entropy change, ΔS_{M} , has a significant value over a broad temperature range – figure 5.10 – with the maximum values located at temperatures very close to the magnetic tran-

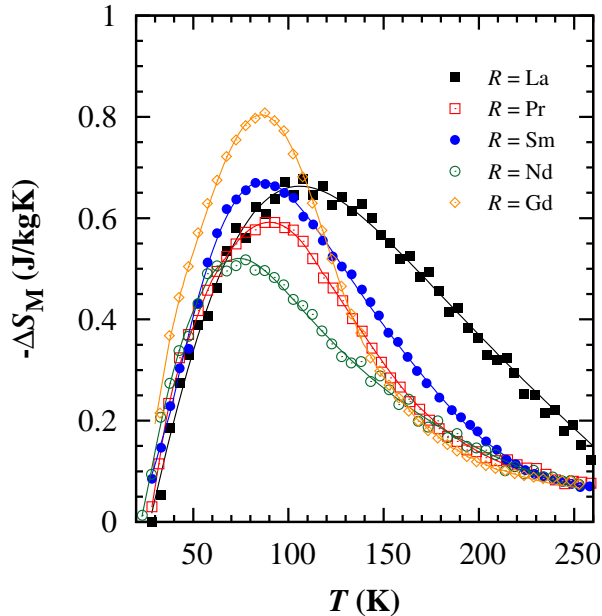


Figure 5.10: Temperature dependences of the magnetic entropy changes for all of the investigated samples for $\mu_0\Delta H = 0\text{-}4$ T.

sition ones. The broadening of the magnetic entropy change versus temperature curves for $T > T_{\text{C}}$ can be attributed to the short-range magnetic order still present. The low maximum $|\Delta S_{\text{M}}|$ values could be explained by the fact that in 4 T the magnetization is far from saturation. The magnetic cooling efficiency was evaluated using equation (3.3) –

Table 5.6: Magnetocaloric parameters for the investigated manganites.

Sample	T_{max} (K)	$ \Delta S_{\text{M}} (\text{max})$ (J/kgK)	δT_{FWHM} (K)	$RCP(S)$ (J/kg)
$\text{La}_{1.4}\text{Ca}_{1.6}\text{Mn}_2\text{O}_7$	107	0.66	154	102
$\text{La}_{1.2}\text{Pr}_{0.2}\text{Ca}_{1.6}\text{Mn}_2\text{O}_7$	90	0.59	111	66
$\text{La}_{1.2}\text{Nd}_{0.2}\text{Ca}_{1.6}\text{Mn}_2\text{O}_7$	74	0.52	114	59
$\text{La}_{1.2}\text{Sm}_{0.2}\text{Ca}_{1.6}\text{Mn}_2\text{O}_7$	86.5	0.67	115	77
$\text{La}_{1.2}\text{Gd}_{0.2}\text{Ca}_{1.6}\text{Mn}_2\text{O}_7$	85.9	0.8	93	74

table 5.6. The $RCP(S)$ values obtained for these compounds are comparable with results previously reported by [99] for $\text{La}_{1.4}\text{Ca}_{1.6}\text{Mn}_2\text{O}_7$ prepared through the sol-gel method [99].

Selected Conclusions

In this work, some physical properties of rare earth-3d transition metal intermetallic compounds and oxides were presented and discussed. Our investigations were focused on the RM_2 and RM_{13} classes of intermetallic compounds and the $\text{La}_{1.4}\text{Ca}_{1.6}\text{Mn}_2\text{O}_7$ double-layered manganites.

We managed to successfully prepare NaZn_{13} -type $\text{La}_{0.7}\text{Nd}_{0.3}\text{Fe}_{13-x}\text{Si}_x$ samples, which were ferromagnetically ordered. The Fe moments at 5 K were quite independent of composition ($2.05 \pm 0.09 \mu_B/\text{atom}$), suggesting a high degree of localization. The Curie temperatures increased almost linearly with Si content, due to a strong s - d orbital hybridization caused by the addition of Si. These compounds showed a changing of the character of the transition at T_C from a first-order (low Si content) to a weak first-order one (high Si content), along with an IEM transition in the paramagnetic region for low Si concentrations. We obtained high magnetocaloric parameters for these compounds (ΔS_M , RCP) which were high enough to consider these materials for magnetic refrigeration applications.

The $\text{HoFe}_{2-x}\text{Al}_x$ compounds were investigated in a wide composition range. These compounds were found to be ferrimagnetically ordered. The Fe-rich samples displayed Curie temperatures in the room-temperature range, while the hexagonal ones showed rather low values for the Curie temperature which decreased with Al content. Electronic structure calculation results showed a good agreement between theory and experiment. All of the investigated compounds showed high RCP values. The low $|\Delta S_M|$ values of the cubic $\text{HoFe}_{2-x}\text{Al}_x$ compounds made them unsuitable for magnetocaloric applications. However, the higher $|\Delta S_M|$ values of the hexagonal compounds made them good candidates for intermediate-region magnetocaloric applications.

The magnetic behaviour of Fe in $\text{Er}_{1-x}\text{Zr}_x\text{Fe}_2$ was investigated. These compounds were found to be ferrimagnetically ordered, with the presence of a compensation point in the $M(T)$ plots. The Curie temperatures increased, while the compensation points decreased with Zr content. The temperature dependences of the spontaneous magnetizations showed a possible rotation of the Er when Zr was added. The Fe moments at 5 K were found to decrease strongly with Zr content, possibly due to band-filling effects or to a possible canted orientation of the Er moments, in which case the Fe moments would have been overestimated. Electronic structure calculation results showed a good agreement between theory and experiment. These compounds displayed rather low $|\Delta S_M|$ values. Large $RCP(\Delta S)$ values due to the wide $\Delta S_M(T)$ curves. Due to their low $|\Delta S_M|$ values, these materials are unsuitable for room-temperature magnetic refrigeration applications.

$\text{La}_{1.4-x}\text{Ce}_x\text{Ca}_{1.6}\text{Mn}_2\text{O}_7$ samples were successfully prepared by using the sol-gel method. The Curie temperatures decreased slowly from around 109 K for $x = 0$ to 100 K for

$x = 0.2$, due to a weakening of the Mn-Mn exchange interaction. The investigated compounds did not saturate even in applied fields up to 12 T, due to the absence of true long-range ferromagnetic order generated by the small grain sizes. An antiferromagnetic alignment of the Ce and Mn moments was suggested, based on the current measurements and previously reported data. An effective moment value of $4.25 \mu_B$ was found for Mn, suggesting the presence of both Mn^{4+} and Mn^{3+} ions, a fact which was confirmed by XPS measurements. These materials were found to undergo a second-order magnetic phase transition at T_C . A moderate magnetocaloric effect was found for both samples, with the maximum entropy changes located at temperatures near T_C .

$La_{1.2}R_{0.2}Ca_{1.6}Mn_2O_7$ ($R = La, Pr, Nd, Sm$ and Gd) samples were synthesized through the sol-gel method. The partial substitution of La with smaller ions increased the inter-layer lattice distortion causing a reduction of the exchange interaction strength. All five samples exhibited clear differences between FC and ZFC magnetizations at low temperatures indicating the presence of a spin-glass like behavior due to frustrations of random competing ferromagnetic and antiferromagnetic interactions together with anisotropy. Magnetic measurements and XPS Mn $3s$ spectra indicated a valence of about 3.65+ for the Mn atoms in all of the investigated samples. Also, it was shown that the Mn effective magnetic moment was not significantly affected by the substitutions. A moderate magnetocaloric effect was found for all of the samples, with the maximum entropy change located at temperatures near the magnetic transition ones.

The high $RCP(S)$ values together with the broadened $\Delta S_M(T)$ curves and the absence of magnetic hysteresis for temperatures higher than 70 K suggested the possibility of using these double layered manganites in magnetic refrigeration devices.

Selected References

- [1] A. M. Tishin *J. Magn. Magn. Mater.*, vol. 316, no. 2, pp. 351 – 357, 2007.
- [2] A. M. Tishin and Y. I. Spichkin, *The Magnetocaloric Effect and its Applications*. Institute of Physics Publishing, Bristol and Philadelphia, 2003.
- [3] K. H. J. Buschow *Rep. Prog. Phys.*, vol. 40, no. 10, p. 1179, 1977.
- [4] E. Burzo, A. Chelkowski, and R. Kirchmayr in *Landolt-Börnstein Numerical Data and Functional Relationships in Science and Technology* (H. P. Wijn, ed.), vol. 9, pp. 172 – 202, Springer-Verlag, 1990.
- [5] J. H. Wernick, “Topologically close-packed structures,” in *Intermetallic Compounds* (J. H. Westbrook, ed.), pp. 197 – 216, John Wiley & Sons, Inc., New York, London, Sydney, 1967.
- [6] K. Momma and F. Izumi *J. Appl. Crystallogr.*, vol. 44, no. 6, pp. 1272 – 1276, 2011.
- [7] M. V. Nevitt, “Miscellaneous structures of fixed stoichiometry,” in *Intermetallic Compounds* (J. H. Westbrook, ed.), pp. 217 – 230, John Wiley & Sons, Inc., New York, London, Sydney, 1967.
- [8] E. C. Stoner *Proc. R. Soc. Lond. A*, vol. 165, pp. 372 – 414, 1938.
- [9] C. J. Howard, B. J. Kennedy, and B. C. Chakoumakos *J. Phys.: Condens. Matter*, vol. 12, no. 4, p. 349, 2000.
- [10] M. R. Levy, *Crystal Structure and Defect Property Predictions in Ceramic Materials*. PhD thesis, Imperial College of Science, Technology and Medicine, Department of Materials, 2005.
- [11] A. Muñoz, J. A. Alonso, M. J. Martínez-Lope, J. L. García-Muñoz, and M. T. Fernández-Díaz *J. Phys.: Condens. Matter*, vol. 12, no. 7, p. 1361, 2000.
- [12] M. Johnsson and P. Lemmens, “Crystallography and chemistry of perovskites,” in *Handbook of Magnetism and Advanced Magnetic Materials*, 2007.
- [13] J. L. García-Muñoz, J. Rodríguez-Carvajal, P. Lacorre, and J. B. Torrance *Phys. Rev. B*, vol. 46, pp. 4414 – 4425, 1992.
- [14] L. Vasylechko, L. Akselrud, W. Morgenroth, U. Bismayer, A. Matkovskii, and D. Savytskii *J. Alloys Compd.*, vol. 297, no. 1 – 2, pp. 46 – 52, 2000.
- [15] C. J. Howard and B. J. Kennedy *J. Phys.: Condens. Matter*, vol. 11, no. 16, p. 3229, 1999.
- [16] T. Hashimoto, N. Tsuzuki, A. Kishi, K. Takagi, K. Tsuda, M. Tanaka, K. Oikawa, T. Kamiyama, K. Yoshida, H. Tagawa, and M. Dokiya *Solid State Ionics*, vol. 132, no. 3 – 4, pp. 181 – 188, 2000.
- [17] Y. Moritomo, A. Asamitsu, H. Kuwahara, and Y. Tokura *Nature*, vol. 380, pp. 141 – 144, 1996.
- [18] S. N. Ruddlesden and P. Popper *Acta Crystallographica*, vol. 11, no. 1, pp. 54–55, 1958.
- [19] J. Mitchell, J. Millburn, M. Medarde, S. Short, J. Jorgensen, and M. T. Fernández-Díaz *J. Solid State Chem.*, vol. 141, no. 2, pp. 599 – 603, 1998.
- [20] J. F. Mitchell, J. E. Millburn, M. Medarde, D. N. Argyriou, and J. D. Jorgensen *J. Appl. Phys.*, vol. 85, p. 4352, 1999.
- [21] H. Meskine, Z. S. Popović, and S. Satpathy *Phys. Rev. B*, vol. 65, p. 094402, 2002.
- [22] N. A. Benedek, A. T. Mulder, and C. J. Fennie *J. Solid State Chem.*, 2012.
- [23] J. M. D. Coey, M. Viret, and S. von Molnár *Adv. Phys.*, vol. 48, no. 2, pp. 167 – 293, 1999.
- [24] C. Zener *Phys. Rev.*, vol. 81, pp. 440 – 444, 1951.
- [25] S. Streule, *Neutron Diffraction Study of Cobaltite Systems*. PhD thesis, Swiss Federal Institute of Technology Zürich, 2006.
- [26] H. A. Kramers *Physica*, vol. 1, no. 1 – 6, pp. 182 – 192, 1934.
- [27] P. W. Anderson *Phys. Rev.*, vol. 79, pp. 350 – 356, 1950.

-
- [28] P. W. Anderson *Phys. Rev.*, vol. 80, pp. 922 – 923, 1950.
- [29] J. B. Goodenough *Phys. Rev.*, vol. 100, pp. 564 – 573, 1955.
- [30] J. Kanamori *J. Phys. Chem. Solids*, vol. 10, no. 2 – 3, pp. 87 – 98, 1959.
- [31] A. Brown and J. H. Westbrook, “Formation techniques,” in *Intermetallic Compounds* (J. H. Westbrook, ed.), pp. 303 – 339, John Wiley & Sons, Inc., New York, London, Sydney, 1967.
- [32] K. Rath *Science and Technology Review*, pp. 24 – 26, May 2005.
- [33] V. R. Galakhov, M. Demeter, S. Bartkowski, M. Neumann, N. A. Ovechkina, E. Z. Kurmaev, N. I. Lobachevskaya, Y. M. Mukovskii, J. Mitchell, and D. L. Ederer *Phys. Rev. B*, vol. 65, p. 113102, 2002.
- [34] E. Beyreuther, S. Grafström, L. M. Eng, C. Thiele, and K. Dörr *Phys. Rev. B*, vol. 73, p. 155425, 2006.
- [35] S. Vosko, L. Wilk, and M. Nusair *Can. J. Phys.*, vol. 58, p. 1200, 1980.
- [36] H. Monkhorst and J. Pack *Phys. Rev. B*, vol. 13, p. 5188, 1976.
- [37] J. S. Faulkner *Prog. Mater. Sci.*, vol. 27, p. 1, 1982.
- [38] J. S. Faulkner and G. M. Stocks *Phys. Rev. B*, vol. 21, p. 3222, 1980.
- [39] J. Lyubina, O. Gutfleisch, M. D. Kuz'min, and M. Richter *J. Magn. Magn. Mater.*, vol. 320, no. 18, pp. 2252 – 2258, 2008.
- [40] M. Ilyn, A. Tishin, F. Hu, J. Gao, J. Sun, and B. Shen *J. Magn. Magn. Mater.*, vol. 290 – 291, Part 1, pp. 712 – 714, 2005.
- [41] F. Wang, G. jun Wang, F. xia Hu, A. Kurbakov, B. gen Shen, and Z. hua Cheng *J. Phys.: Condens. Matter*, vol. 15, no. 30, p. 5269, 2003.
- [42] S. Fujieda, A. Fujita, and K. Fukamichi *Appl. Phys. Lett.*, vol. 81, p. 1276, 2002.
- [43] A. K. Pathak, P. Basnyat, I. Dubenko, S. Stadler, and N. Ali *J. Magn. Magn. Mater.*, vol. 322, no. 6, pp. 692 – 697, 2010.
- [44] H. Zhang, Y. Long, Q. Cao, Y. Mudryk, M. Zou, K. G. Jr., and V. Pecharsky *J. Magn. Magn. Mater.*, vol. 322, no. 13, pp. 1710 – 1714, 2010.
- [45] F. X. Hu, B. G. Shen, J. R. Sun, and Z. H. Cheng *Appl. Phys. Lett.*, vol. 78, p. 3675, 2001.
- [46] F. X. Hu, M. Ilyn, A. M. Tishin, J. R. Sun, G. J. Wang, Y. F. Chen, F. Wang, Z. H. Cheng, and B. G. Shen *J. Appl. Phys.*, vol. 93, p. 5503, 2003.
- [47] T. Liu, Y. Chen, Y. Tang, S. Xiao, E. Zhang, and J. Wang *J. Alloys Compd.*, vol. 475, no. 1–2, pp. 672 – 675, 2009.
- [48] B. R. Hansen, L. T. Kuhn, C. Bahl, M. Lundberg, C. Ancona-Torres, and M. Katter *J. Magn. Magn. Mater.*, vol. 322, no. 21, pp. 3447 – 3454, 2010.
- [49] M. Balli, M. Rosca, D. Fruchart, and D. Gignoux *J. Magn. Magn. Mater.*, vol. 321, no. 2, pp. 123 – 125, 2009.
- [50] B. G. Shen, J. R. Sun, F. X. Hu, H. W. Zhang, and Z. H. Cheng *Adv. Mater.*, vol. 21, no. 45, pp. 4545 – 4564, 2009.
- [51] T. Palstra, J. Mydosh, G. Nieuwenhuys, A. van der Kraan, and K. Buschow *J. Magn. Magn. Mater.*, vol. 36, no. 3, pp. 290 – 296, 1983.
- [52] J. Shen, Y.-X. Li, J. Zhang, B. Gao, F.-X. Hu, H.-W. Zhang, Y.-Z. Chen, C.-B. Rong, , and J.-R. Sun *J. Appl. Phys.*, vol. 103, p. 07B317, 2008.
- [53] H. Hamdeh, H. Al-Ghanem, W. Hikal, S. Taher, J. Ho, D. Anh, N. Thuy, N. Duc, and P. Thang *J. Magn. Magn. Mater.*, vol. 269, no. 3, pp. 404 – 409, 2004.
- [54] J. Shen, Q.-Y. Dong, Y.-X. Li, and J.-R. Sun *J. Alloys Compd.*, vol. 458, no. 1 – 2, pp. 115 – 118, 2008.

-
- [55] G.-J. Wang, F. Wang, N.-L. Di, B.-G. Shen, and Z.-H. Cheng *J. Magn. Magn. Mater.*, vol. 303, no. 1, pp. 84 – 91, 2006.
- [56] P. Mohn and E. P. Wohlfarth *J. Phys. F: Metal Phys.*, vol. 17, no. 12, p. 2421, 1987.
- [57] M.-K. Han and G. J. Miller *Inorg. Chem.*, vol. 47, pp. 515 – 528, 2008.
- [58] J. Shen, B. Gao, Q.-Y. Dong, Y.-X. Li, F.-X. Hu, J.-R. Sun, and B.-G. Shen *J. Phys. D: Appl. Phys.*, vol. 41, no. 24, p. 245005, 2008.
- [59] L. Jia, J. R. Sun, F. W. Wang, T. Y. Zhao, H. W. Zhang, B. G. Shen, D. X. Li, S. Nimori, Y. Ren, and Q. S. Zeng *Appl. Phys. Lett.*, vol. 92, p. 101904, 2008.
- [60] O. Tegus, E. Brück, L. Zhang, Dagula, K. Buschow, and F. de Boer *Physica B: Condens. Matter*, vol. 319, no. 1 – 4, pp. 174 – 192, 2002.
- [61] T. Zhang, Y. Chen, and Y. Tang *J. Phys. D: Appl. Phys.*, vol. 40, no. 18, p. 5778, 2007.
- [62] T. Hashimoto, K. Matsumoto, T. Kurihara, T. Numazawa, A. Tomokiyo, H. Yayama, T. Goto, S. Todo, and M. Sahashi *Adv. Cryog. Eng.*, vol. 32, p. 279, 1986.
- [63] M. Ilyn, A. Tishin, V. Pecharsky, A. Pecharsky, and K. Gschneidner Jr. *Cryogenic Engineering and International Cryogenic Materials Conference, July 16-20, Madison, Wisconsin*, 2001.
- [64] M. A. Laguna-Marco, J. Chaboy, and C. Piquer *Phys. Rev. B*, vol. 77, p. 125132, 2008.
- [65] E. Burzo *Solid State Commun.*, vol. 14, no. 12, pp. 1295 – 1298, 1974.
- [66] R. Grössinger, W. Steiner, and K. Krec *J. Magn. Magn. Mater.*, vol. 2, no. 1 – 3, pp. 196 – 202, 1976.
- [67] A. E. Dwight, C. W. Kimball, R. S. Preston, S. P. Taneja, and L. Weber *J. Less-Common Met.*, vol. 40, no. 3, pp. 285 – 291, 1975.
- [68] H. Oesterreicher *J. Appl. Phys.*, vol. 42, no. 12, pp. 5137 – 5143, 1971.
- [69] H. Oesterreicher and R. Pitts *J. Appl. Phys.*, vol. 43, no. 12, pp. 5174 – 5179, 1972.
- [70] H. Fuess, D. Givord, A. R. Gregory, and J. Schweizer *J. Appl. Phys.*, vol. 50, pp. 2000 – 2002, 1979.
- [71] E. Burzo *Z. Angew. Phys.*, vol. 32, p. 127, 1971.
- [72] M. S. S. Brooks, L. Nordstrom, and B. Johansson *J. Phys.: Condens. Matter*, vol. 3, no. 14, p. 2357, 1991.
- [73] H. Maletta, G. Crecelius, and W. Zinn *Proc. Mössbauer Conference (Bendorf)*, 1974.
- [74] K. G. Sandeman *Scripta Mater.*, vol. 67, no. 6, pp. 566 – 571, 2012.
- [75] R. Tetean, E. Burzo, I. G. Deac, V. Pop, and D. Benea *J. Magn. Magn. Mater.*, vol. 316, no. 2, pp. e387 – e389, 2007.
- [76] M. O. Bargouth and G. Will *J. Phys. Colloques*, vol. 32, pp. C1-675 – C1-676, 1971.
- [77] K. Ikeda and T. Nakamichi *J. Phys. Soc. Jpn.*, vol. 39, no. 4, pp. 963 – 968, 1975.
- [78] G. E. Fish, J. J. Rhyne, S. G. Sankar, and W. E. Wallace *J. Appl. Phys.*, vol. 50, p. 2003, 1979.
- [79] S. A. Nikitin, E. V. Talalaeva, L. A. Chernikova, and A. S. Andreenko *J. Eksp. Teor. Phys.*, vol. 62, p. 2058, 1973.
- [80] T. G. Perring, G. Aeppli, Y. Moritomo, and Y. Tokura *Phys. Rev. Lett.*, vol. 78, pp. 3197 – 3200, 1997.
- [81] H. Asano, J. Hayakawa, and M. Matsui *Phys. Rev. B*, vol. 56, pp. 5395 – 5403, 1997.
- [82] Y. Moritomo, Y. Maruyama, T. Akimoto, and A. Nakamura *Phys. Rev. B*, vol. 56, pp. R7057 – R7060, 1997.
- [83] N. H. Hur, J.-T. Kim, K. H. Yoo, Y. K. Park, J.-C. Park, E. O. Chi, and Y. U. Kwon *Phys. Rev. B*, vol. 57, pp. 10740 – 10744, 1998.
- [84] T. Kimura and Y. Tokura *Annu. Rev. Mater. Sci.*, vol. 30, pp. 451 – 457, 2000.
- [85] I. D. Fawcett, E. Kim, M. Greenblatt, M. Croft, and L. A. Bendersky *Phys. Rev. B*, vol. 62, pp. 6485

- 6495, 2000.
- [86] S. Chatterjee, P. H. Chou, C. F. Chang, I. P. Hong, and H. D. Yang *Phys. Rev. B*, vol. 61, pp. 6106 – 6113, 2000.
- [87] C. D. Ling, J. E. Millburn, J. F. Mitchell, D. N. Argyriou, J. Linton, and H. N. Bordallo *Phys. Rev. B*, vol. 62, pp. 15096 – 15111, 2000.
- [88] A. I. Coldea, S. J. Blundell, C. A. Steer, J. F. Mitchell, and F. L. Pratt *Phys. Rev. Lett.*, vol. 89, p. 277601, 2002.
- [89] G. Allodi, M. Bimbi, R. De Renzi, C. Baumann, M. Apostu, R. Suryanarayanan, and A. Revcolevschi *Phys. Rev. B*, vol. 78, p. 064420, 2008.
- [90] H. Asano, J. Hayakawa, and M. Matsui *Appl. Phys. Lett.*, vol. 68, pp. 3638 – 3641, 1996.
- [91] H. Asano, J. Hayakawa, and M. Matsui *Appl. Phys. Lett.*, vol. 70, pp. 2303 – 2306, 1997.
- [92] D. N. Argyriou, J. F. Mitchell, P. G. Radaelli, H. N. Bordallo, D. E. Cox, M. Medarde, and J. D. Jorgensen *Phys. Rev. B*, vol. 59, pp. 8695 – 8702, 1999.
- [93] T. J. Zhou, Z. Yu, W. Zhong, X. N. Xu, H. H. Zhang, and Y. W. Du *J. Appl. Phys.*, vol. 85, p. 7975, 1999.
- [94] A. Wang, G. Cao, Y. Liu, Y. Long, Y. Li, Z. Feng, and J. R. Jr. *J. Appl. Phys.*, vol. 97, pp. 103906 – 103909, 2005.
- [95] K. Cherif, S. Zemni, J. Dhahri, M. Oumezzine, M. Said, and H. Vincent *J. Alloys Compd.*, vol. 432, no. 1 – 2, pp. 30 – 33, 2007.
- [96] H. Zhu, H. Song, and Y. Zhang *Appl. Phys. Lett.*, vol. 81, pp. 3416 – 3419, 2002.
- [97] X. Zhao, W. Chen, Y. Zong, S. Diao, X. Yan, and M. Zhu *J. Alloys Compd.*, vol. 469, no. 1 – 2, pp. 61 – 65, 2009.
- [98] R. Tetean, C. Himcinschi, and E. Burzo *J. Optoelectron. Adv. Mater.*, vol. 10, pp. 849 – 852, 2008.
- [99] E. Taşarkuyu, A. Coşkun, A. Irmak, S. Aktürk, G. Ünlü, Y. Samancıoğlu, A. Yücel, C. Sarkürkçü, S. Aksoy, and M. Acet *J. Alloys Compd.*, vol. 509, no. 9, pp. 3717 – 3722, 2011.
- [100] K. Zhou, Y. Zhuang, J. Li, J. Deng, and Q. Zhu *Solid State Commun.*, vol. 137, no. 5, pp. 275 – 277, 2006.
- [101] H. Asano, J. Hayakawa, and M. Matsui *Phys. Rev. B*, vol. 57, pp. 1052 – 1056, 1998.
- [102] J. Q. Li, C. Q. Jin, and H. B. Zhao *Phys. Rev. B*, vol. 64, p. 020405, 2001.
- [103] T.-J. Zhou, Z. Yu, W. Zhong, X. N. Xu, H. H. Zhang, and Y. W. Du *J. Appl. Phys.*, vol. 85, pp. 7975 – 7978, 1999.
- [104] R. Dudric, F. Goga, M. Neumann, S. Mican, and R. Tetean *J. Mater. Sci.*, vol. 47, pp. 3125 – 3130, 2012.
- [105] T. Kimura, Y. Tomioka, H. Kuwahara, A. Asamitsu, M. Tamura, and Y. Tokura *Science*, vol. 274, pp. 1698 – 1701, 1996.
- [106] A. Maignan, C. Martin, G. Van Tendeloo, M. Hervieu, and B. Raveau *Phys. Rev. B*, vol. 60, pp. 15214 – 15219, 1999.
- [107] J. Dho, W. S. Kim, and N. H. Hur *Phys. Rev. B*, vol. 65, p. 024404, 2001.
- [108] D. A. Shirley *Phys. Rev. B*, vol. 5, pp. 4709 – 4714, 1972.

List of Publications

1. *Magnetocaloric effect in $La_{1.2}R_{0.2}Ca_{1.6}Mn_2O_7$ compounds*
R. Tetean, C. Himcinschi, A. Vlădescu, **S. Mican**
Journal of Optoelectronics and Advanced Materials, 13 (3), 263 – 267 (2011);
2. *Magnetic properties and magnetocaloric effect in $La_{1.4-x}Ce_xCa_{1.6}Mn_2O_7$ perovskites synthesized by sol-gel method*
R. Dudric, F. Goga, M. Neumann, **S. Mican** and R. Tetean
Journal of Materials Science, 47, 3125 – 3130 (2011);
3. *Magnetic properties and magnetocaloric effect in $La_{0.7}Nd_{0.3}Fe_{13-x}Si_x$ compounds*
S. Mican and R. Tetean
Journal of Solid State Chemistry, 187, 238 – 243 (2012);
4. *The effect of Gd doping on electronic properties of NiMnSb compounds*
R. Grasin, C. Rusu, R. Dudric, **S. Mican**, M. Neumann and R. Tetean
Journal of Optoelectronics and Advanced Materials - Rapid Communications, 6, 169 – 173 (2012);
5. *Electronic and magnetic properties of $NiMn_{1-x}Ho_xSb$ compounds*
R. Grasin, C. Rusu, A. Laslo, R. Dudric, **S. Mican**, M. Neumann and R. Tetean
Physica Status Solidi (b), 249 (9), 1779 – 1783 (2012);
6. *Magnetism and large magnetocaloric effect in $HoFe_{2-x}Al_x$*
S. Mican, D. Benea and R. Tetean
Journal of Alloys and Compounds, <http://dx.doi.org/10.1016/j.jallcom.2012.09.009>;

List of Conference Contributions

1. Joint European Magnetic Symposia (JEMS) 2010, 23-28 August 2010, Krakow, Poland
Magnetic properties and magnetocaloric effect in $La_{0.7}Nd_{0.3}Fe_{13-x}Si_x$ compounds
S. Mican and R. Tetean
2. 2nd EuroMagNET Summer School "Science in High Magnetic Fields", 5-11 September 2010, Ameland, Netherlands
Magnetic properties of $Tb_8Co_{16-x}M_x$ compounds where $M = Cu$ or Al
S. Mican, A. Bezerghéanu, C. Rusu, I. G. Deac and R. Tetean
3. The European Conference Physics on Magnetism 2011 (PM'11), 27 June - July 1, Poznan, Poland
Magnetic properties and electronic structure of $La_{1.2}Nd_{0.2}Ca_{1.6}Mn_2O_7$ and $La_{1.2}Sm_{0.2}Ca_{1.6}Mn_2O_7$ compounds
R. Dudric, **S. Mican**, C. Himcinschi and R. Tetean
4. The European Conference Physics on Magnetism 2011 (PM'11), 27 June - July 1, Poznan, Poland
Magnetic behaviour of iron in $Er_{1-x}Zr_xFe_2$ compounds
S. Mican, D. Benea, O. Ginsca, I.G. Deac and R. Tetean
5. The European Conference Physics on Magnetism 2011 (PM'11), 27 June - July 1, Poznan, Poland
Magnetic properties and magnetocaloric effect of $HoCo_{3-x}Al_x$ compounds
A. Bezerghéanu, C. Rusu, R. Grasin, **S. Mican**, I.G. Deac and R. Tetean
6. The European Conference Physics on Magnetism 2011 (PM'11), 27 June - July 1, Poznan, Poland
Magnetotransport properties of $La_{0.55}Ca_{0.45}MnO_3/BaTiO_3$ composites
M. Kiss, A. Vladescu, I. Balasz, O. Florea, A. Tunyagi, **S. Mican**, R. Tetean and I.G. Deac
7. The European School on Magnetism – "Time-Dependent Phenomena in Magnetism", 22 August - 2 September 2011, Târgoviște, Romania
Structural and magnetic properties of $Ho_8Fe_{16-x}Al_x$ compounds
S. Mican and R. Tetean

8. Joint European Magnetic Symposia (JEMS) 2012, 9-14 September, Parma, Italy
Magnetism and large magnetocaloric effect in $\text{HoFe}_{2-x}\text{Al}_x$ compounds
S. Mican, D. Benea and R. Tetean

Acknowledgements

First, I would like to acknowledge the PhD scholarship granted to me through the Sectoral Operational Programme for Human Resources Development 2007-2013, co-financed by the European Social Fund, under the project POSDRU 88/1.5/S/60185 – “Innovative Doctoral Studies in a Knowledge Based Society”.

I would like to adress my deep thanks to my scientific supervisor, Prof. Dr. Romulus Tetean for the constant guidance and encouragement in these three years of doctoral studies. The numerous discussions I’ve had with him regarding scientific data, along with the countless suggestions and discussions in the process of writing scientific papers, progress reports and the PhD thesis have proven to invaluable in the course of my study. He encouraged me to be independent in my research and in writing scientific papers, preparing posters and presentations.

I also express my deep thanks to Conf. Dr. Iosif Deac for the invaluable help and insight regarding the experimental setups and for the numerous discussions in the field of magnetism.

I would also like to express my appreciation to Prof. Dr. Liviu Chioncel (Augsburg Center for Innovative Technologies, University of Augsburg, Germany), who supervised me in the four months of my research stage there. I would like to thank him for his valuable insight, the countless discussions regarding electronic structure calculations and his constant encouragement into understanding the principles behind these calculation methods.

My special thanks go to Dr. Eugen Dorolti for his help in preparing the intermetallic samples and in performing heat treatments. I also would like to thank Dr. Roxana Dudric for her valuable insight regarding perovskite materials and the numerous discussions we’ve had in the field of magnetism. I would like to express my thanks to Dr. Diana Benea for performing the KKR electronic structure calculations.

I also thank my family for their continued financial and moral support and for their permanent trust and continuous encouragements during my studies.